On the variability of the slow solar wind: New insights from the modelling and *PSP-WISPR* observations.

Nicolas Poirier[1,2], Victor Réville[3], Alexis P. Rouillard[3], Athanasios Kouloumvakos[4], and Emeline Valette[3]

[1] Rosseland Centre for Solar Physics, University of Oslo, Postboks 1029 Blindern, N-0315 Oslo, Norway
[2] Institute of Theoretical Astrophysics, University of Oslo, Postboks 1029 Blindern, N-0315 Oslo, Norway
[3] IRAP, Université Toulouse III - Paul Sabatier, CNRS, CNES, Toulouse, France
[4] The Johns Hopkins University Applied Physics Laboratory, 11101 Johns Hopkins Road, Laurel, MD 20723, USA

July 12, 2023

ABSTRACT

Aims. We analyse the signature and origin of transient structures embedded in the slow solar wind, and observed by the *Wide-Field Imager for Parker Solar Probe* (*WISPR*) during its first 10 passages close to the Sun. *WISPR* provides a new in-depth vision on these structures, which have long been speculated to be a remnant of the pinch-off magnetic reconnection occurring at the tip of helmet streamers.

Methods. We pursue the previous modelling works of Réville et al. (2020, 2022) that simulate the dynamic release of quasi-periodic density structures into the slow wind through a tearing-induced magnetic reconnection at the tip of helmet streamers. Synthetic *WISPR* white-light (WL) images are produced using a newly developed advanced forward modelling algorithm, that includes an adaptive grid refinement to resolve the smallest transient structures in the simulations. We analyse the aspect and properties of the simulated WL signatures in several case studies, typical of solar minimum and near-maximum configurations.

Results. Quasi-periodic density structures associated with small-scale magnetic flux ropes are formed by tearing-induced magnetic reconnection at the heliospheric current sheet and within $3 - 7$ R$_\odot$. Their appearance in WL images is greatly affected by the shape of the streamer belt and the presence of pseudo-streamers. The simulations show periodicities on the $\simeq 90 - 180$ min, $\simeq 7 - 10$ hr and $\simeq 25 - 50$ hr timescales, which are compatible with *WISPR* and past observations.

Conclusions. This work shows strong evidence for a tearing-induced magnetic reconnection contributing to the long-observed high variability of the slow solar wind.

Key words. Sun: solar wind – Methods: numerical – Methods: observational – Magnetohydrodynamics (MHD) – Instabilities – Magnetic reconnection

1. Introduction

In contrast to the fast solar wind, a mystery remains on the origin of the slow solar wind (SSW) and of its high variability. This variability can be the result of 'time-dependent' and/or 'spatial-dependent' effects.

The spatial-dependent variability often emerges in structured bundles of bright rays in coronal white-light (WL) emissions, that have long been observed from coronagraphs and heliospheric imagers such as the *Solar and Heliospheric Observatory* (SoHO: Domingo et al. 1995) and the *Solar TErrestrial RElations Observatory* (STEREO: Kaiser et al. 2008). Recently, the *Wide-Field Imager for Parker Solar Probe* (WISPR: Vourlidas et al. 2016) unveiled a finer structuring of the slow solar wind at scales down to the thin heliospheric plasma sheet (HPS) (Poirier et al. 2020; Liewer et al. 2022; Howard et al. 2022).

On the other hand, it has been shown that the SSW is also highly time-dependent, by hosting up to $\approx 80\%$ of quasi-periodic structures Viall et al. (2008). This paper focus on the time-dependent variability of the slow wind, as captured from the *WISPR* novel perspective and in light of state-of-the-art modelling.

Density transient structures that propagate along with the SSW have long been observed in white-light imagery, with a great variety of shapes, speed, and origins.

Among the most evident ones one could mention coronal mass ejections (CMEs), which by releasing tremendous amount of coronal material into the heliosphere, generate significant brightness enhancements in both coronagraph and heliospheric images (see e.g. the review by Webb & Howard 2012). Some CME events that undergo more moderate and progressive accelerations, so called streamer blowouts, have been particularly observed to deflect towards the cusp of helmet streamers and further propagate within the SSW (see e.g. the recent *WISPR* observations described in Hess et al. 2020; Korreck et al. 2020; Rouillard et al. 2020c).

Since the beginnings of the *SoHO-LASCO* coronagraph, other CME-like flux rope structures known as the 'Sheeley blobs' (Sheeley et al. 1997) have been observed to propagate along the bright rays associated with streamer stalks where the densest slow wind originates. First interpretations suggested that these structures formed as a result of a pinch-off reconnection at the tip of helmet streamers that would have been stretched out beforehand (Gosling et al. 1995; Wang et al. 1998), the conditions leading to this stretching and eventually to the reconnection remaining still unclear. In some occasions, they also appear as bright arches, which may be more or less squashed according to their inclination with the observer (see e.g. Sheeley & Rouillard 2010).

In fact, large loops from active regions (ARs) have also been observed to leave arch-like signatures as they gradually expand into the corona (as seen in both X-ray and WL emissions, see Uchida et al. 1992; Morgan et al. 2013). A helmet streamer made of such expanding loops may then be prone to stretching, and to the formation of streamer blobs via the pinch-off reconnection scenario.

This picture has the advantage to be also consistent with observations of plasma inflows in *LASCO* (Wang et al. 2000; Sheeley & Wang 2002), which have been associated for the first time with outflowing blobs later on (Sanchez-Diaz et al. 2017b; Lynch 2020). The continuous tracking of blobs expelled from the tip of helmet streamers all the way to points of in situ measurements reveals that they transport helical magnetic fields (Rouillard et al. 2009b, 2011), which is further supported by recent *Parker Solar Probe* (*PSP*) observations (Lavraud et al. 2020; Rouillard et al. 2020a). More systematic statistical analyses based on *STEREO* images, and of in situ measurements inside the HPS revealed that the topology of blobs is consistent with magnetic flux ropes (Sanchez-Diaz et al. 2019) that could form via magnetic reconnection at the tip of helmet streamers (Sanchez-Diaz et al. 2017a).

The modelling of streamer instabilities in time-dependent magnetohydrodynamics (MHD) simulations also supports this scenario (Chen et al. 2009; Lynch 2020). Following in the footsteps of these models, Réville et al. (2020) investigated in detail the tearing instability that occurs near the cusp of streamers, in a high-resolution 2.5D simulation of the corona and using an idealistic dipolar configuration of the solar magnetic field. Streamer blobs were reproduced, in addition to a plethora of quasi-periodic structures over a wide range of frequencies. Indeed, past studies based on near 1 AU remote-sensing and in situ observations also reveal the existence of quasi-periodic structures with periodicities varying from $\approx 90 - 180$ min to $\approx 8 - 16$ hr (Viall et al. 2010; Viall & Vourlidas 2015; Kepko et al. 2016; Sanchez-Diaz et al. 2017b), which were found in recent *PSP* observations as well (Rouillard et al. 2020a). From a high-cadence campaign on the *STEREO-A COR-2* coronagraph, (DeForest et al. 2018) recently unveiled the ubiquitous presence of density fluctuations at even smaller scales $\approx 20 - 40 - 60$ min.

In addition to the density and magnetic field, other plasma properties have also been measured to vary during the passage of these transients. For instance, Kepko et al. (2016) showed a similarity between the variability of the charge state ratios measured in situ in the slow wind and the short, hourly time scale of the quasi-periodic structures observed remotely in WL streamers. This SSW originating from streamers tends to exhibit high charge state ratios typical of hot AR, whereas the SSW that emerges further away from streamers, probably from deeper inside coronal holes is characterized by lower charge-state ratios comparable to those measured in the fast wind (Neugebauer et al. 2002; Liewer et al. 2004; Stakhiv et al. 2015, 2016). The 'streamer-like' SSW is also known to be more enriched in heavy ions having a low first ionisation potential (FIP) (see e.g. von Steiger 1996; Peter 1998), a composition typical of closed-field plasma from ARs (see e.g. Ko et al. 2002; Brooks & Warren 2011; Doschek & Warren 2019). The streamer-like SSW, or at least its dynamic component, could hence be conveniently interpreted as originating from the pinch-off reconnection mechanism, by offering a channel through which closed-field material can be intermittently released into the slow wind.

This paper further investigates this scenario through a qualitative comparison between the recent highly-resolved WL observations taken by *WISPR*, and high-resolution simulations of the solar corona and solar wind. We first analyse in section 2, two events observed by *WISPR* which depict quasi-periodic structures. We then present, in Sect. 3, our modelling approach to reproduce such structures through the tearing-induced reconnection at the tip of streamers. Synthetic *WISPR* images are then produced and compared against observations in Sect. 4. Limitations and future perspectives on this work are discussed in Sect. 5. We finally conclude on the possible implications of this work to the understanding of the slow solar wind in Sect. 6.

2. Observations

After its first 11 successful encounters *WISPR* have already provided a wealth of images rich in structures that were often unresolved from typical 1 AU observatories (see e.g. Howard et al. 2022, for an overview of the 10th encounter). That is a direct benefit of bringing an imager as close to the Sun, at a vantage point that is located inside the corona. By drastically shortening the line-of-sight integration path, *WISPR* is able to resolve with unprecedented detail the density structures that propagate within the slow solar wind. *WISPR* consists of two WL heliospheric imagers that are mounted on the ram side of *PSP*, and so the solar wind structures can be imaged prior to their in situ measurement (Vourlidas et al. 2016). *WISPR* offers a large field-of-view (FOV) thanks to its two telescopes, which cover in elongation angle (ϵ, angle away from the Sun) $13.5 - 53.0°$ for the inner (*WISPR-I*) and $50.5 - 108.5°$ for the outer (*WISPR-O*) telescope. At the closest approach to be reached by *PSP* in 2024 (9.86 R$_\odot$), *WISPR-I* will be able to observe the corona from only 2.3 R$_\odot$. We exploit *WISPR* level-3 images[1] which have been calibrated (see Hess et al. 2021) and where contributions to the white-light emissions by dust particles (i.e. the F-corona) have been subtracted to unveil only the faint K-corona made up of coronal electrons (see Howard et al. 2022, for more details on the procedure).

2.1. First insights on the transients observed by WISPR

WISPR has detected a wealth of fluctuations in the slow wind, whose signatures can be very diverse. Among these fluctuations many have been associated to magnetic flux ropes with a clear dark cavity, suggesting that these flux ropes have likely been observed edge-on or at a small inclination angle.

We present two examples of such signatures in Fig. 1, captured by the inner telescope *WISPR-I* during the 8th *PSP* encounter. Two bright shells (green arrows) can be seen, one being circular (bottom panel) while the other being more 'v-shaped' (top panel). Such shapes have already been observed from 1 AU, albeit to a larger spatial extent. They have been especially captured in great detail in events associated with pristine slow CMEs observed by *WISPR*. The v-shape had been either interpreted as a slight inclination of the flux rope with respect to the line-of-sight (LOS) of the observer or as a byproduct of the reconnection process itself that generates the flux rope (Thernisien & Howard 2006; Rouillard et al. 2009a, 2020c). The fact that the brightness enhancement is often more marked at the back end of the flux rope supports the latter scenario, by an accumulation of plasma

---

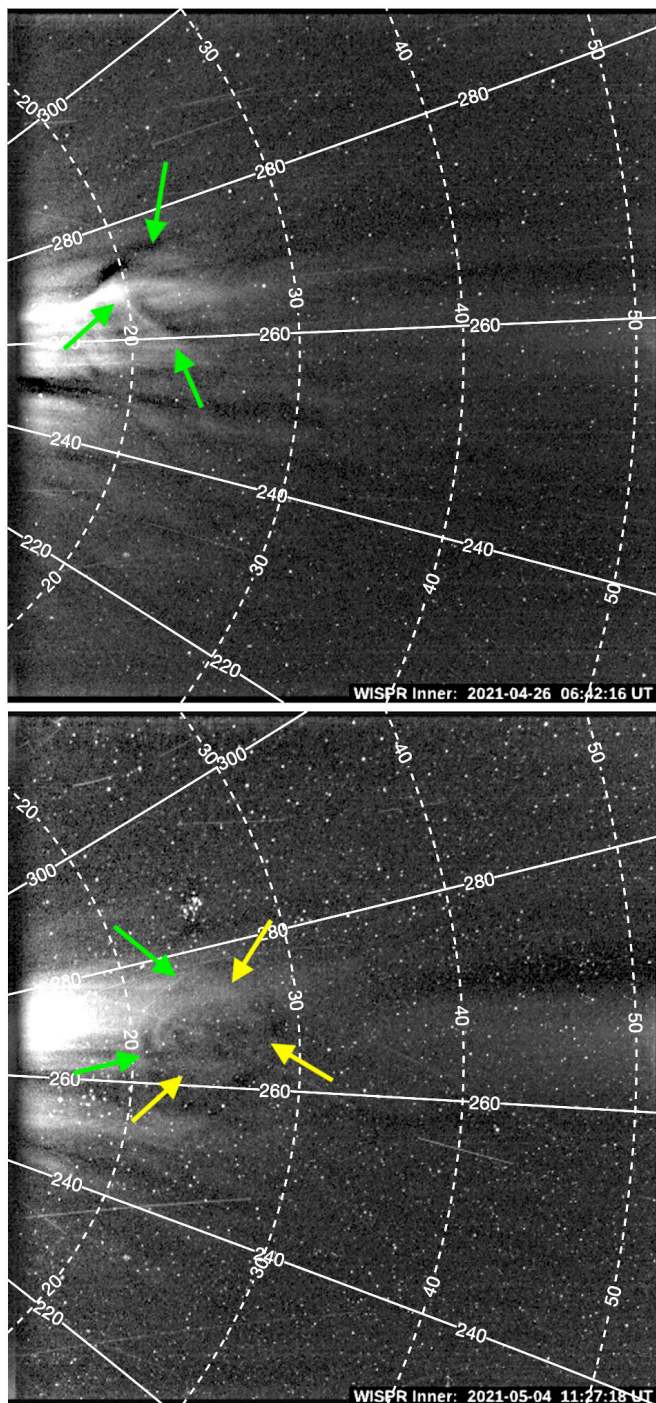[1] data source: https://wispr.nrl.navy.mil/wisprdata

Fig. 1. Two examples of large-scale density structures observed by *WISPR-I* on April-26 2021, 06:42 universal time (UT, top panel) and May-04 2021, 11:27 UT (bottom panel). The Helioprojective-Radial coordinate grid is plotted as solid white isolines for the position angle (i.e. the counter-clockwise angle from solar north) and dashed white isolines for the elongation angle (ϵ), both in degrees.

Fig. 2. Two examples of small-scale density structures observed by *WISPR-I* on April-26 2021, 22:57 UT (top) and March-01 2022, 15:15 UT (bottom). The Helioprojective-Radial coordinate grid is again represented with the same format as in Fig. 1. The green lines represent the pixels extracted to build the time-distance (J-)maps shown in Fig. 4.

from the reconnection exhaust. With a closer look at the bottom panel of Fig. 1, one can also see an inner circular structure (yellow arrows), which has also been detected in other transients observed by *WISPR* (see e.g. Hess et al. 2020; Rouillard et al. 2020c; Howard et al. 2022).

Most signatures of this scale have been found to be associated with sporadic (slow) CME events, where flux ropes are already present low in the corona well below the tip of streamers
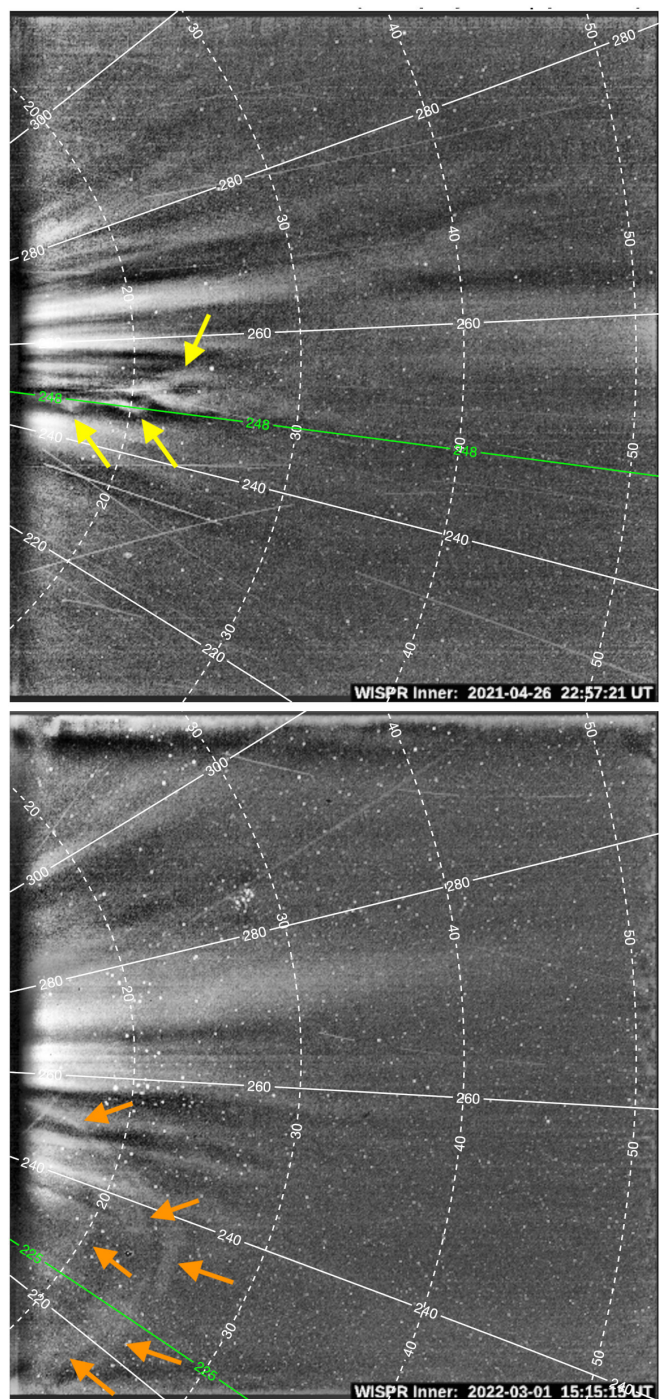
(see e.g. Hess et al. 2020; Korreck et al. 2020; Rouillard et al. 2020c; Howard et al. 2022). In this paper we focus on flux ropes that form on a regular basis just above the tip of helmet streamers, which are presumed to be major contributors to the variability of the slow wind.

Compared to past near 1 AU observations, the novelty of *WISPR* observations is in imaging streamers from much closer in, providing clearer signatures of its embedded transients and

access to smaller scales. In figure 2, we show two events that may be related to quasi-periodic structures captured by *WISPR-I* during the 8th (top panel) and 11th (bottom panel) *PSP* encounters, hereafter referred as the April-2021 and March-2022 events respectively. We could identify a series of other similar events in *WISPR-I* images, but we only selected here the most visible ones for illustrative purposes, particularly in the most recent *WISPR-I* observations. Although more difficult to interpret because of a higher solar activity, they unveil local features that clearly stand out from the background signal.

The top panel unveils a track of three small-scale structures. Similarly to the larger scale events shown previously in Fig. 1, they also appear as bright annulus suggesting flux ropes seen edge-on (green arrows). At this point it is hard to say whether these structures are actual small-scale flux ropes or if that is because they are located far away from *WISPR*, that will be discussed later on. In contrast, the bottom panel shows arch-like signatures (orange arrows). Similar signatures have already been observed from 1 AU, and have been related to flux ropes seen with a greater inclination angle or almost face-on (Sheeley & Rouillard 2010; Rouillard et al. 2011), or also to expanding AR loops (Morgan et al. 2013). In the latter case though, the expansion of the loops is much slower than the propagation speed of the transients captured by *WISPR* (see the fitting performed in Sect. 2.3).

Similarly to the April-2021 event shown in the top panel, a close-up visual inspection of the March-2022 event also reveals consecutive arches following each other. Both these events show interesting periodic behaviour in their spatial distribution, and hence they may be connected to the above-mentioned $90 - 180$ min quasi-periodic structures that have been previously detected in the slow wind, that will be discussed further in Sect. 2.3.

Finally, we can give a rough estimate of the brightness variation induced by the passage of these transients. For this purpose, we examined the pixel values as given in unit of mean solar brightness ($B_\odot$) in the level-3 *WISPR-I .fits* files. It is important to notice that these data products are not photometrically accurate, because some of the K-corona emissions might be removed during the background removal procedure[2]. We averaged the emissions over representative areas that define the transients and the background (host) streamers, and computed the relative difference $(\bar{B}_{transient} - \bar{B}_{streamer})/\bar{B}_{streamer}$. We found relative brightness increases of $\approx 80 - 95\%$ for the April-2021 (edge-on case) event and $\approx 30 - 50\%$ for the March-2022 (face-on case) event. That is brighter than what has been typically measured from 1 AU for the Sheeley et al. (1997)'s blobs. As we shall see throughout this paper, the Sheeley blobs and the quasi-periodic structures captured by *WISPR* can be related to two different families of transients produced by pinch-off reconnection at the tip of helmet streamers.

2.2. Global context from near 1 AU observations

To get a better context for these events, we construct WL maps of the streamer belt as observed from near 1 AU by *LASCO-C2* over half a solar rotation. We show these maps in Fig. 3 (b and d panels). Estimates of the Heliospheric Current Sheet (HCS) derived from Potential Field Source Surface (PFSS) extrapolations are plotted (as red dashed lines) to help us differentiate pseudo-streamers (unipolar structures) from

the main streamer belt (where the magnetic polarity switches sign). Assuming that the above transients originate from and propagate within the streamer belt, we could identify two possible source regions that have an inclination consistent with the April-2021 and March-2022 events observed by *WISPR*. Since the imaged transients significantly stand out from the background streamers, they should be located quite close to the Thomson sphere (see the magenta lines) where most of the WL emissions are expected to originate (see Sect. 3.3). As such we identified two possible source regions, a nearly aligned section of the streamer belt located within $60 - 110°$ (and $\approx 0°$, see panel b) of Carrington longitudes (and latitudes), and an inclined section of the streamer belt located within $220 - 280°$ (and $- 20 - 0°$, see panel d).

The low-coronal structures underlying the streamer belt, as observed in extreme ultraviolet (EUV) by the Atmospheric Imaging Assembly (*AIA*) equipped on the Solar Dynamics Observatory (*SDO*), are shown in panel a and c of Fig. 3.

In panel c, two major ARs can be clearly seen at longitudes $210°$ and $245°$, which are located underneath the potential source streamer that produced the March-2022 event. Such ARs may prove important in the formation of streamer transients. The hot plasma in such active closed-field regions can be prone to expansion into the corona through thermal instability, bringing the AR loops that are frozen into that plasma to higher coronal heights, eventually up to the cusp of streamers. On the other hand in panel a, no significant AR is visible beneath the streamer that potentially produced the April-2021 event observed by *WISPR*. However, it has also been suggested that the stretching of streamers can naturally occur simply as the result of the magnetic field near the cusp being too weak to hold the thermal pressure exerted by the underlying plasma Chen et al. (2009).

Both mechanisms could act in pair for the formation of streamer transients through the pinch-off reconnection process, which are actually supported by both observations (see e.g. Morgan et al. 2013) and simulations (Chen et al. 2009; Réville et al. 2020). In particular, we will see in the results section (4.1) that the pinch-off reconnection process can generate transients with a low frequency that is quite variable and dependent on the local coronal conditions beneath the streamer. Therefore, the presence and amount of ARs beneath streamers could implicitly affect the rate at which these low-frequency transients are produced. From past observations near 1 AU, such transients have been detected with periods varying from $\approx 8-16$ hr (Sanchez-Diaz et al. 2017a, near solar maximum) to $0.5 - 2$ days (Morgan 2021, near solar minimum). A future statistical study that links such heliospheric measurements to low-atmospheric EUV observations would be helpful to better assess the contribution of ARs on the release of streamer transients.

2.3. Tracking transients in WISPR J-maps

A usual and efficient method to further characterise transient features and have more insights into their possible generation mechanism is by measuring their periodicity. For this purpose, a method that has been widely used across the community is to track transients in distance-time maps called 'J-maps' (see e.g. Sheeley et al. 1999, 2008; Rouillard et al. 2008, 2009b). The bright features that appear in such J-maps then provide insightful information on the periodicity, propagation speed and acceleration profiles of such transients (to some limitations as discussed below).

---

[2] see the disclaimer about the level-3 (version 1) data at https://wispr.nrl.navy.mil/wisprdata
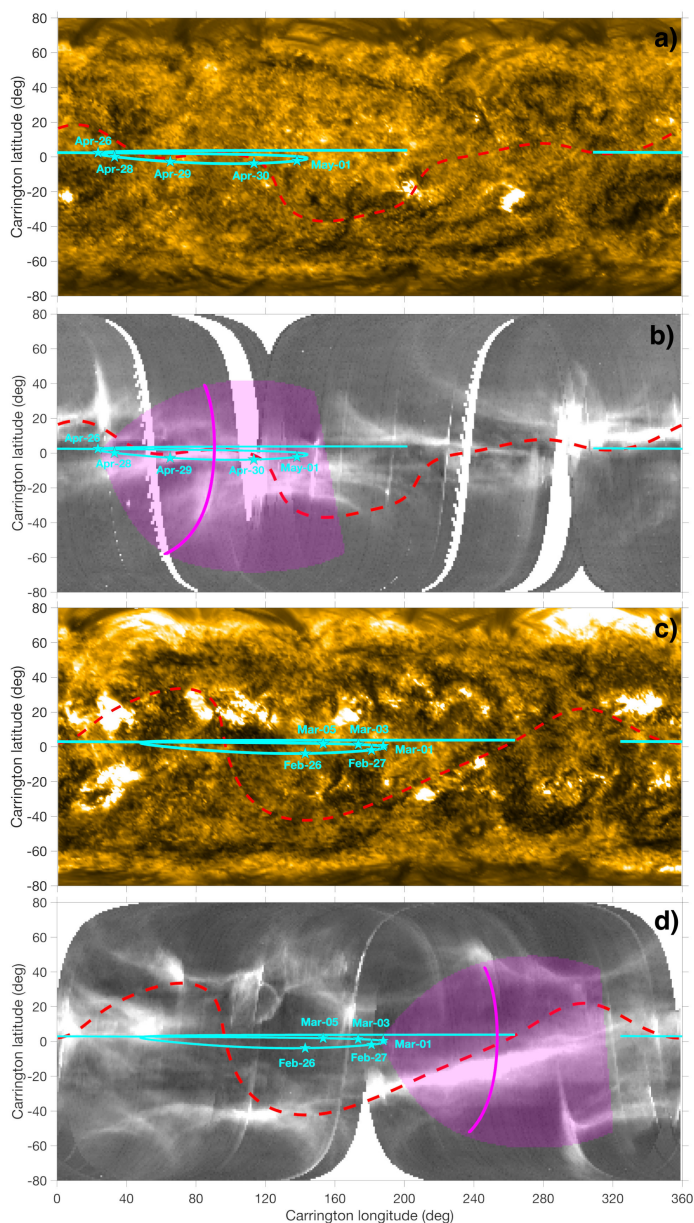
Fig. 3. Panel a and c: synoptic maps of the low solar atmosphere derived from *SDO-AIA* (171Å) EUV observations. Panel b and d: synoptic maps of the WL corona as seen from near 1 AU by the *SoHO LASCO-C2* coronagraph. These maps have been produced by combining on-disk (off-limb) images over a full (half) solar rotation prior to the April-26 2021 (panels a and b) and March-01 2022 (panels c and d) events (see section 4.2 of Rouillard et al. 2020b, for a description of the method). The dashed red line represents an estimate of the shape of the HCS derived from PFSS extrapolations of the photospheric magnetic field. Among the multitude of photospheric maps available we picked two maps that match both, the shape of the WL streamer belt (see Poirier et al. 2021) and timings of HCS crossings determined from magnetic sector measurements taken in situ at *PSP*. In the present case, the magnetic maps from the Air force Data Assimilative Flux Transport (ADAPT) model (Arge et al. 2010; Arge et al. 2011, 2013) for April-16 12:00UT (8th realization) and March-01 12:00UT (11th realization) have been selected assuming a source surface height of 2.0 R$_\odot$ and 2.5 R$_\odot$ respectively. The vertical (radial) projection of *PSP* orbit onto the solar disk is plotted in cyan colour with star symbols marking several dates at *PSP*. The magenta surfaces represent the projections of the regions scanned by *WISPR-I* at the time of the two images shown in Fig. 2, with a solid line indicating the location of the Thomson sphere extracted at $\epsilon = 22°$.

Such maps are commonly produced by extracting pixels along a fixed direction (either at the ecliptic or at another position angle), and using the elongation angle (ϵ) as a measure of the angular distance away from Sun centre.

Tracking transient features in heliospheric images has long been a delicate task, and even more for a rapidly-moving and up-close imager as *WISPR*. To this end, new techniques have been developed to better track *WISPR* features, whether they are static (e.g. coronal rays: Liewer et al. 2022) or dynamic (e.g. CMEs: Liewer et al. 2020). These techniques include a number of corrections to account for instance, for the effects of spacecraft motion, perspective, and orbit out of the solar equatorial plane. For instance, a transient propagating radially outwards from the Sun does not necessarily remain at a constant position angle as it moves across the *WISPR* FOV, and its distance to *WISPR* may also vary. That can affect their appearance in J-maps. For instance, curved signatures were noted during a CME event that came close to the two heliospheric imagers onboard *STEREO* (Sheeley et al. 2008; Rouillard et al. 2008). Furthermore, when a target moves away from the observer, hence leading to an 'apparent' slowing of its propagation speed, that can also produce curved signatures in J-maps as we will see later for the April-2021 event. Performing a precise fitting of the transients observed by *WISPR* is out the scope of this study, and hence circumvents the need of a complex tracking technique as developed by Liewer et al. (2022).

The J-maps associated to the March-2022 and April-2021 events introduced earlier are shown in Fig. 4. The corresponding slits along which the J-maps have been constructed are plotted in Fig. 2 as green lines. These J-maps are classical distance-time maps except that instead of the typical elongation angle that measures the angle away from Sun centre, the radial distance to the Sun is used. The implicit assumption to determine this parameter however, is that extracted pixels are projected onto the Thomson sphere, a reference surface where WL emissions are expected to be strongest (see discussion in Sect. 3.3).

From these J-maps we could infer some insightful properties of the transient structures captured by *WISPR*, which we describe in the following paragraphs.

Propagation profiles
Such Jmaps allow us to perform a direct visual inspection of the speed profile of the propagating structures. For this purpose we fitted profiles of constant speed (dashed red lines) for several of the most visible stripes. We note that several substructures could also be seen in between some of the brightest fronts, but were too faint to be shown here. The March-2022 event (right panel) is fairly well described by constant speed profiles at ≈ 415 km/s. In contrast, the April-2021 event (left panel) shows curved stripes that deviate from constant speed profiles, and with a very low speed (≈ 160 km/s). Although such a low propagation speed could be due to perspective effects (e.g. of the transients moving away from *WISPR*), we show in Sect. 2.4 that this is probably here associated to a very slow and dense slow solar wind flow within the HPS.

Curved signatures in Jmaps have already been noticed in *STEREO* observations for instance (Sheeley et al. 2008; Rouillard et al. 2008) and also more recently in *WISPR* (Howard et al. 2022). These apparent decelerations were in fact associated to the effect of the imaged structures getting closer to or away from the observer. Since *PSP* remained relatively 'static' (i.e. co-rotating with the solar corona) at that time, that might suggest that the structure itself was moving with respect to *WISPR*. That
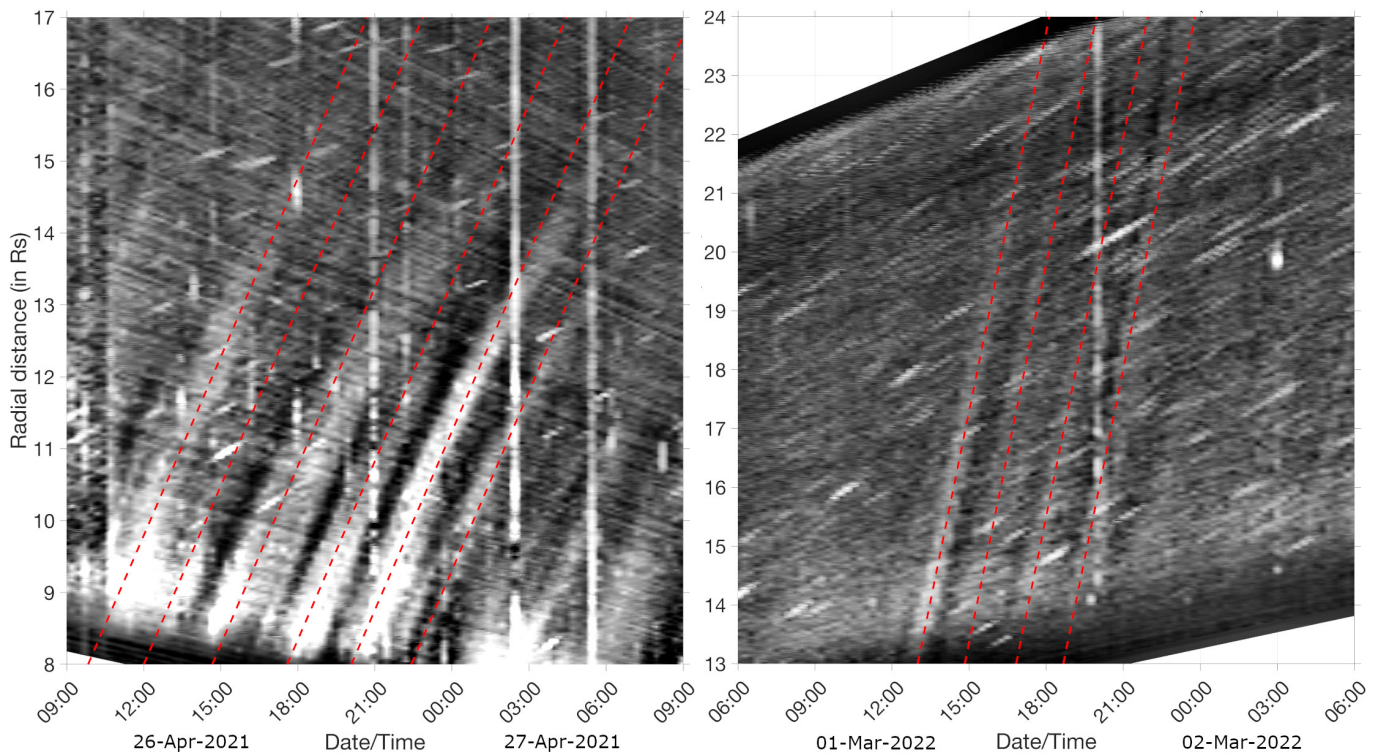
Fig. 4. *WISPR-I* distance-time (J-)maps for the April-2021 (left) and March-2022 (right) events, and along the two slits shown in Fig. 2 (solid green lines). Fitted profiles are plotted as dashed red lines, with constant velocity of 160 km/s (left) and 415 km/s (right), i.e. about the solar wind bulk velocity measured a few days later by *PSP-SWEAP/SPC* in situ (see Fig. 5).

is also consistent with the WL signatures that suggest flux ropes propagate along *PSP* orbital plane (see the green dashed line in the top panel of Fig. 2), where the legs of these flux ropes may have come closer or away from *WISPR* during their expansion. The pinch-off reconnection mechanism at the tip of streamers indeed predicts that such flux ropes develop large azimuthal extents, from their generation and during their expansion in the solar wind (Sanchez-Diaz et al. 2019).

Periodicities

The periodicities measured between the fitted stripes range from $\approx 110 - 120$ min (left panel) and $\approx 130 - 175$ min (right panel) in between the fitted stripes. That falls well within the typical $\approx 90 - 180$ min range previously detected from near 1 AU observations. Furthermore, similar periodicities are also retrieved in an upcoming statistical study from Viall & Vourlidas (2023) that includes a few *PSP* encounters. Because of the rapidly varying viewing conditions of *WISPR*, quasi-corotation phases do not last very long and hence periodicities above ≈ 10 hr cannot easily be detected. Therefore it remains difficult to check whether the longer $\approx 8 - 16$ hr periods of streamer blobs measured previously from slowly moving 1 AU observatories also manifests in *WISPR* images.

As we will see in the next section, such periodicities could be byproducts of the pinch-off reconnection process occurring at the tip of streamers, and more precisely the manifestation of multiple modes associated to the tearing instability that can develop at the HCS.

2.4. Insights from plasma measurements taken in situ at PSP

We check whether the low propagation speeds measured for the April-26 2021 event imaged by *WISPR-I* are realistic, by making

a rough comparison with the solar wind speeds measured in situ at *PSP* around that time, as shown in Fig. 5. This is possible because after that event, *PSP* entered in a pro-grade phase and hence could a few days later sample a solar wind channel that probably hosted the transients captured by *WISPR-I* (see the *PSP* orbit plotted in the top panel of Fig. 3).

On the top panel, one can see that the *Solar Probe Analyzer* (*SPAN*) instrument, that is part of the *Solar Wind Electrons Alphas and Protons* (SWEAP: Kasper et al. 2016) investigation on board *PSP*, indeed measured very slow (purple dots) and dense (emerald green dots) solar wind with $\approx 160 - 250$ km/s and $\approx 1 - 8 \times 10^3$ 1/cc at around 15 $R_\odot$. Such plasma flows are typical of coronal streamers at that distance (Cho et al. 2018; Morgan & Cook 2020), and more generally of HPS (see e.g. Winterhalter et al. 1994; Sanchez-Diaz et al. 2019; Lavraud et al. 2020), that is also supported by a few HCS crossings during this interval (here simply identified by a global polarity inversion of the magnetic field, see middle panel). Such SSW are hence potential hosts of blobs and quasi-periodic structures as those observed by *WISPR-I*. Unfortunately in this case, the transients imaged by *WISPR-I* on April-26 (located within $\approx 8 - 16$ $R_\odot$) already moved far away before *PSP* could get inside that streamer belt starting from April-29. Nevertheless, the solar wind velocities measured there (at ≈ 15 $R_\odot$, see the top and bottom panels of Fig. 5) match well with the ≈ 160 km/s fitted speed of the imaged transients.

3. Modelling: Method

Several main characteristics of transients in the slow wind have been extracted from *WISPR* observations. Now we introduce in this section our modelling approach to get more insights on the
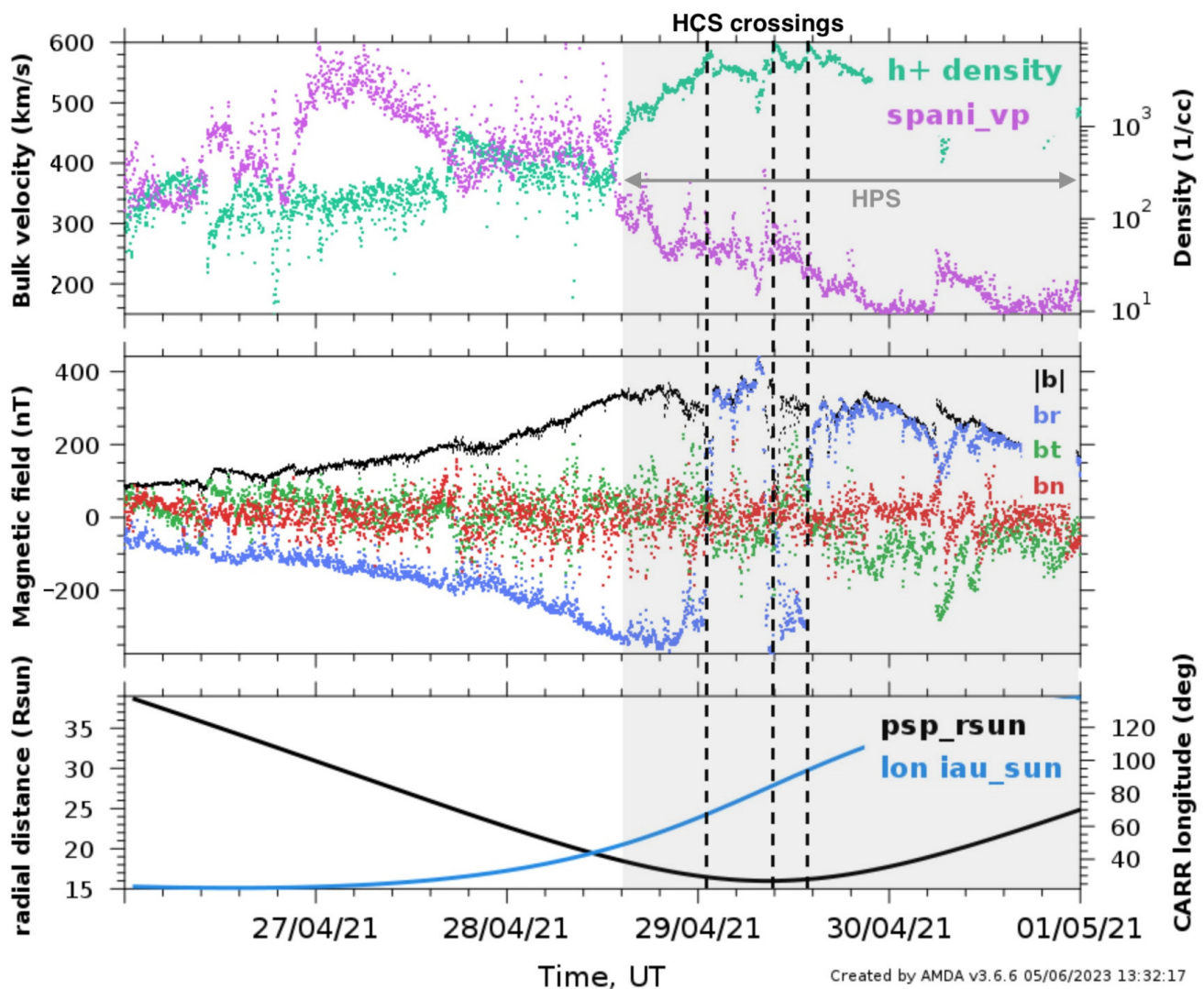
Fig. 5. Top panel: bulk velocity (left axis) and density of the proton solar wind measured by the *PSP-SPANi*. Middle panel: Magnetic field (1-min average) measured by the *PSP-FIELDS* magnetometer (*MAG*). Bottom panel: radial distance to the Sun and Carrington longitude of *PSP*. A few days after the April-2021 event observed by *WISPR-I*, *PSP* sampled a very dense and slow solar wind typical of HPS, with several magnetic polarity inversions suggesting potential crossings of the HCS. Figure produced with the *AMDA* web tool publicly available at (http://amda.irap.omp.eu/).

possible origin of these structures. We will test the idea that the pinch-off reconnection process at the tip of streamers is responsible for the formation and release of the small transients observed by *WISPR*.

This mechanism is tested in, first an idealistic simulation of a very high resolution time-dependent 2.5-D MHD dipolar corona (Sect. 3.1), and then a lower resolution time-dependent 3-D MHD simulation of the conditions encountered by *PSP* during its 9th passage near the Sun (Sect. 3.2). We then present in Sect. 3.3 our approach to building synthetic products that can be compared with *WISPR* observations.

3.1. Idealistic simulation of a dipolar corona

Réville et al. (2020) describe in detail the pinch-off reconnection mechanism induced by the tearing instability, in an idealistic 2.5-D simulation of the solar corona. To allow a fair comparison with actual observations from *WISPR*, the Réville et al. (2020)'s simulation has been rerun with more outputs (one every $\simeq$ 13 min) to match the typical temporal cadence of *WISPR*.

In figure 6 we illustrate the main phases of the pinch-off reconnection mechanism, with several snapshots extracted from the simulation and zoomed-in views on the left-hand side panels. Starting from a near equilibrium state ($t = 0$ min, 1st row), the tip of the helmet streamer eventually expands ($t = 1540$ min, 2nd row) due to pressure imbalance between the closed-field plasma confined beneath (such as in coronal loops) and the out-flowing plasma from the adjacent open-field. As the helmet streamer expands a thinning also occurs at its back end, up to a point where the streamer gets sufficiently thin locally for the tearing instability to trigger magnetic reconnection ($t = 2349.8$ min, 3rd row), referred as 'the ballooning mode' in Réville et al. (2020). The ejecta of a large plasmoid of dense and initially closed-field material follows ($t = 2880.8$ min, 4th row). The tearing instability further develops at smaller scales triggering reconnection at multiple secondary sites, that is 'the tearing mode'. Plasma material is pushed away from these reconnection sites and then accumulate in small-scale and dense plasmoids. More precisely, this plasma concentrates in shell-like structures where the magnetic field is mostly poloidal as in magnetic flux ropes. In contrast, the
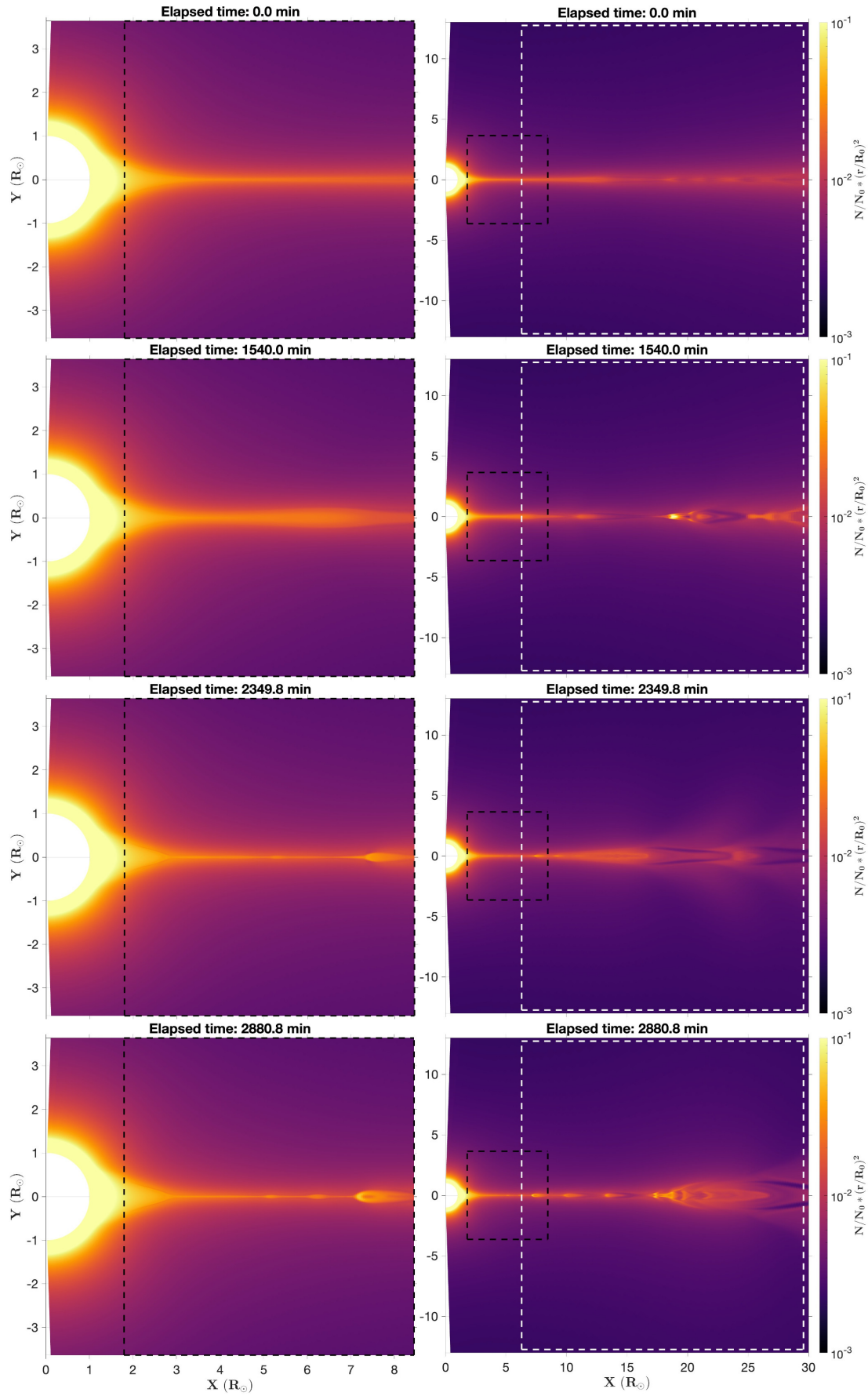
Fig. 6. Simulated electron density from the idealistic dipolar setup. Colours are plotted in a logarithmic scale. The approximate FOV of *WISPR-I* when *PSP* is located at 10 R$_\odot$ and 35 R$_\odot$ is depicted by a dark and white dashed rectangle respectively. An animated version of this figure is available online at https://doi.org/10.5281/zenodo.8135596.

core of these structures is less dense due to a dominant toroidal magnetic field component (i.e. directed across the figure plane). The reader is strongly encouraged to visualize the animation associated to Fig. 6 available online[3], as well as those presented in the original Réville et al. (2020) paper.

For the first time, the inner and outer *WISPR* telescopes combined can provide an in-depth view of the transient structures that form from pinch-off reconnection, right in their formation region. As illustrated in figure 6, *WISPR* may see different signatures according to its distance to the Sun, where the dashed white and dark rectangles show the approximate *WISPR-I* FOV assuming that *PSP* is located at 35 R$_\odot$ and 10 R$_\odot$ from the Sun respectively (10 R$_\odot$ being an estimate of the closest approach to be reached by 2024). For instance, it happens that some of the simulated transients eventually merge together along their propagation to form larger and/or denser plasmoids (see e.g. the lower left panel of Fig. 6). Hence, we pursue here the work of Réville et al. (2020) to examine how such simulated structures may look in a white-light imager as *WISPR*.

To produce synthetic white-light observables, we need first to extend the 2.5-D simulated domain into three dimensions. We hence perform an axisymmetric demultiplication of the 2.5-D simulation about the solar rotation axis, hence producing a 3-D corona with a flat streamer belt at the equator. By changing the position of our virtual observer we can then test most situations encountered by *WISPR* along its orbits and more generally throughout the solar cycle, that is, from a horizontal to vertical streamer belt configuration typical of a solar minimum and maximum respectively.

3.2. Case study simulation of the 9th PSP encounter

Because the 2.5-D setup presented in Réville et al. (2020) is highly idealistic, an attempt has been made to extend this work in a full-fledged 3-D model that is called WindPredict-AW (the reader is refered to Parenti et al. 2022; Réville et al. 2022, for a detailed description). In such modelling framework, the 2.5-D magnetic structures mentioned above translate into 3-D magnetic flux ropes, where their generation and propagation can now be studied in a self-consistent manner. The cons, however, is that the 3-D setup cannot afford a high level of refinement as in the 2.5-D setup. Since magnetic reconnection is allowed by numerical diffusion of the numerical scheme itself, it is bound by the actual numerical size of the mesh near the HCS. The 3-D setup is hence not optimal for the full development of the tearing instability as in the idealistic setup (see Réville et al. 2022, for more details). Despite this limitation the 3-D simulation still does produce transients but at low frequency, which are the ballooning modes and only the quasi-periodic structures with periods $\gtrsim$ 4 hr. By applying a realistic photospheric magnetic map at the inner boundary, Réville et al. (2022) could even reproduce the statistical occurrence of streamer flux ropes that intersected both *PSP* and *SolO* during the joint observation campaign of June 2020.

We here pursue the work of Réville et al. (2022) with a similar 3-D simulation setup but applied to the 9th *PSP* encounter (August 2021). The inner boundary is set with the GONG-ADAPT (11th realization) magnetogram of August-14 2021, 00:00 UT, and kept fixed over the entire simulated period. The magnetogram was selected among many different sources

and dates to best match the observed shape and location of the streamer belt, as seen from 1 AU by *SoHO-LASCO* over a full solar rotation. The selection process is based on the method presented in Poirier et al. (2021). Another criteria was also the correct prediction of both magnetic sectors and timing of HCS crossings measured in situ by *PSP*. Once the simulation relaxed, outputs of the entire 3-D simulated domain have been extracted every $\simeq$ 13 min to match the actual cadence of *WISPR*. For the sake of computational time the simulation was run until 100 outputs were obtained, that covers a time interval of $\simeq$ 22 hr starting at perihelion. The simulation is kept fixed outside this interval, that allows us to synthesize *WISPR* images over a longer period even though the simulated solar wind remains static. Indeed the static phase is still meaningful to differentiate the effect of the fast-moving probe from the propagation of the solar wind structures within the synthesized images. The procedure to produce *WISPR* synthetic images is described in Sect. 3.3.

The simulated streamer belt and density structures propagating within its core are shown in Fig. 7, along with the FOV of both *WISPR-I (white colours)* and *WISPR-O (grey colours)*. At that time *WISPR* was imaging from a distance of $\approx$ 26 R$_\odot$, a highly warped streamer belt typical of a high solar activity. Throughout the region scanned by *WISPR*, the streamer belt undergoes significant latitudinal shifts within $\approx$ -15 $-$ 25° of Carrington latitude. A few flux rope structures have been identified in the simulation (see the coloured arrows). All of them except the farthest one (cyan arrow) will produce visible WL signatures in the synthetic *WISPR* images, that will be presented later in Sect. 4.2. The flux ropes have different extents and widths that may be explained by a different stage of their formation/evolution. One can also notice that the spatial extent of these flux ropes within the streamer belt varies, and that it is delimited by intersections of pseudo-streamers with the main streamer belt (see also Réville et al. 2022). That makes up a complex network that is inherently connected to the so-called S-web (or web of separatrix and quasi-separatrix layers, see Antiochos et al. 2011). Finally, each of these flux ropes show a different inclination. All of that will affect their appearance from the *WISPR* perspective as we shall see in Sect. 4.2.

3.3. Producing synthetic WISPR images

Synthetic *WISPR* images are produced similarly to what has been previously done in Poirier et al. (2020), except that in the present work, not static but time-dependent simulations are used.

Following the Thomson scattering theory (Howard & Tappin 2009; Howard & DeForest 2012), the total intensity received by a pixel detector from scattered electrons can be expressed as an integral along the path length z along each LOS:

$$I_t^{tot} = \int_{z=0}^{z\to+\infty} I_t dz = \int_{z=0}^{z\to+\infty} n_e z^2 G dz \quad \text{(in W.m}^{-2}\text{.sr}^{-1}\text{)}$$

$$G = \frac{B_\odot \pi \sigma_e}{2z^2} \left(\underbrace{2}_{1} \underbrace{[(1-u)C + uD]}_{2} - \underbrace{\sin\chi^2}_{1} \underbrace{[(1-u)A + uB]}_{2} \right)$$

(1)

where I_t refers to the total (and not polarized) intensity, $B_\odot \simeq 2.3 \times 10^7$ W.m^{-2}.sr^{-1} the Sun's mean radiance (or surface brightness) and $\sigma_e = r_e^2 \simeq 7.95 \times 10^{-30}$ m^2 the electron cross-section.
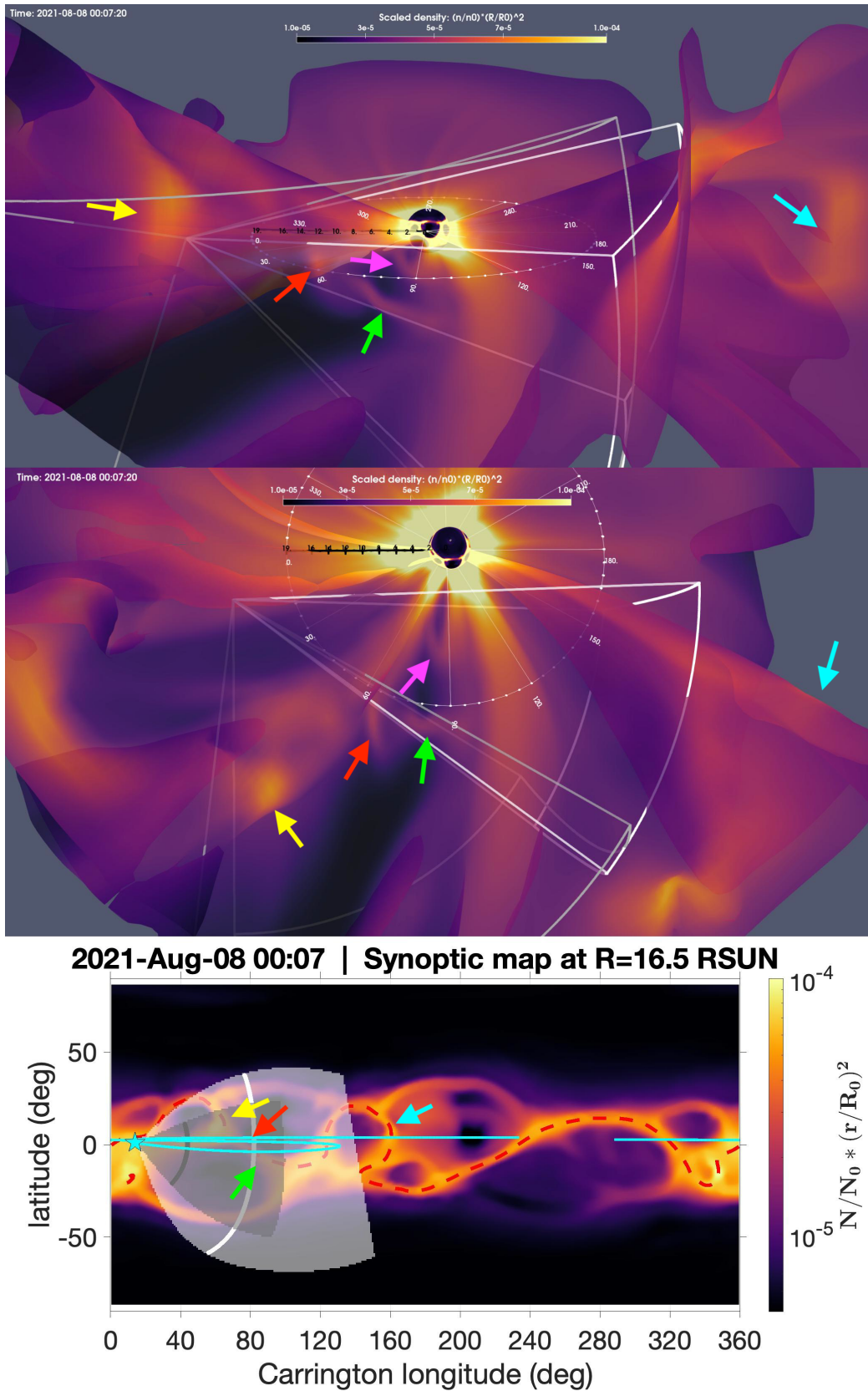

Fig. 7. Simulated density structures from the WindPredict-AW full-fledged 3-D MHD model. Two upper panels: front and top view of the 3-D density structures propagating within the core of the (true) streamer belt (identified with a $Br = 0$ isosurface). Coordinates in the Carrington frame are also given, for the longitudes (white colour, in degrees) and radial distances (dark colour, in solar radii). Bottom panel: synoptic (Carrington) map at $r = 16.5$ R$_\odot$ with *PSP* orbit plotted in cyan colour. To identify the true streamer belt from pseudo-streamer structures, a $Br = 0$ contour is plotted as a red dashed line. In both panels the FOV of *WISPR-I* and *WISPR-O* are shown in white and grey colours respectively. In both panels, the logarithmic colour scale represents the flux of plasma density scaled by its value at the inner boundary ($r = 1.0002$ R$_\odot$). The coloured arrows point to flux rope structures that are discussed in the core text. An animated version of this figure is available online at https://doi.org/10.5281/zenodo.8135596.

The electron density n_e is an input 3-D datacube interpolated at each LOS points. The G function here includes contributions from both pure-geometric scattering (indicated by 1) and the solar illumination function (indicated by 2). For far distances to the Sun, G can be approximated as $(R_\odot/r)^2(2 - \sin\chi^2) = (R_\odot/r)^2(1 + \cos\chi^2)$, where χ is called the scattering angle between the scattering site and the Sun-observer line, and $(R_\odot/r)^2$ represents the classical fall-off of sunlight with heliocentric distance r (see Howard & DeForest 2012). But for an observer as close to the Sun as *WISPR*, one should consider additional effects such as the collimation of sunlight and limb-darkening, using for instance the *van de Hulst* coefficients A, B, C and D defined in Howard & Tappin (2009, eq 25-28). A direct observation of Eq. (1) shows that the integral is semi-infinite on the path length z. In practise one can shrink this integral to a limited (finite) region that includes most contributions to the total brightness, that is discussed in Appendix A.

Theoretical works have shown that one would expect WL emissions produced from Thomson scattering to peak at a surface called the 'Thomson sphere' (TS, Vourlidas & Howard 2006). The latter can be geometrically defined by a sphere with its centre located half way along the Sun-observer line, and with the length of this line for diameter. However, Howard & Tappin (2009) and Howard & DeForest (2012) have demonstrated that this 'peak' at the Thomson sphere is greatly smeared out. Therefore, a detector such as *WISPR* would not be only sensitive to electrons that are concentrated near the Thomson sphere, but rather to a much broader region on either side of the Thomson sphere ($\approx \chi_{TS} \pm 45°$) that is called the 'Thomson plateau' (TP, Howard & DeForest 2012). An illustration of this effect for *WISPR* is given in Poirier et al. (2020, figure 14).

Although there already exists several numerical implementations of this theory within the scientific community (e.g. in the *FORWARD* tool: Gibson et al. 2016), we opted to develop a new algorithm that we can tailor to the specific constrains of *WISPR* and the needs of this study. The procedure is summarised below:

1. *Instrument definition*:
   Given both ephemeris (positioning) and pointing information for our virtual instrument, we build a 2-D matrix of LOS coordinates. To do so, the synthesized image is projected on a reference surface that we choose to be the Thomson sphere.

2. *Grid optimisation*:
   A dynamic grid refinement algorithm adjusts the sampling along each LOS, so that to capture at best the smallest physical structures in the simulation box (see Appendix A). The sample points are distributed from *PSP*, pass through and beyond the Thomson surface. For the *WISPR* images synthesized in this work, that represents 241 million of sample points to be optimised.

3. *Thomson scattering computation*:
   Given a 3-D simulated datacube of electron density, the Thomson scattering formula (1) is computed at each sample point. That includes beforehand an interpolation step that can be very costly, given the large number of sample points and the size of the input datacubes used in this work ($(n_r, n_\theta, n_\phi) = (768, 384, 360)$ and $(256, 160, 320)$ for the idealistic and full-fledged 3-D setup respectively).

4. *LOS integration*:
   The synthesized image is finally obtained by summing up all local contributions to the total brightness along each LOS.

WISPR is a detector placed on a rapidly moving observatory sweeping extended regions of the solar corona in only a few days, together with a rapid variation of its distance to the Sun. The *WISPR* FOV must therefore be updated very regularly, that is done by rerunning phase 1 and 2 also for every single image to be synthesized. As *WISPR* is also much closer to the imaged coronal structures, it is critical to keep an accurate tracking of *WISPR*'s pointing through usage of the World Coordinate System (WCS). For this purpose, the phase 1 exploits the *IDL* routines provided by the *WISPR* instrument team through the *SolarSoft* library.

For the idealistic dipolar numerical setup though, we opted for a simple user-defined FOV that we can easily control to test different scenario as in a sandbox. That allows us to simulate various viewing conditions that *WISPR-I* have encountered (or may in the future) at distinct phases of the solar cycle. We define a FOV representative of *WISPR-I* in the helioprojective-cartesian frame with $HPLN = (10, 50)°$(azimuthal angle) and $HPLT = (−20, 20)°$(elevation angle) where $(HPLN = 0, HPLT = 0)$ points towards solar centre. We suppose a null roll angle for simplicity. The helioprojective frame is a sphere centred at the observer position, which needs to be defined as well. We assumed a *PSP*-Sun distance of 35 $R_\odot$ and 10 $R_\odot$, the first being an average between the March-2022 and April-2021 events presented earlier, and the second being intended to represent the closest approach that *PSP* will ever reach in 2024. The remaining parameter is the latitude of our virtual observer (the longitude does not matter since the idealistic simulation is axisymmetric about the solar rotation axis). Varying the latitude θ allows us to mimic different inclination of the streamer belt from *WISPR* perspective, where large (or small) θ (in absolute value) are intended to be representative of, a streamer belt seen face-on (or edge-on) as during solar maximum (or minimum) conditions. An inclination angle θ of 0° and -40° has been assumed, for comparison with the April-2021 and March-2022 event respectively.

4. Modelling: Results

4.1. Idealistic simulation of a dipolar corona

In Appendix B we gather the raw (absolute brightness) synthetic *WISPR* images produced from the idealistic dipolar modelling setup introduced in 3.1. To enhance the visibility of transient structures, we follow the base difference method where a background image (here computed as the average brightness over the entire time interval) is subtracted to each individual image. The resulting base-difference synthetic images are shown in Figs. 8-9, where bright or dark colours correspond to either an enhancement or depletion in electron density with respect to the background solar wind. These base-difference images reveal faint brightness variations much better. And thanks to the new adaptive grid refinement method developed for this paper, small-scale density structures are rendered with great precision. That manifests as very smooth brightness variations across the LOS, where otherwise sharpness would have indicated an inappropriate sampling along the LOS. One may even notice some small spurious features (especially in the $\theta = -40°$ case). These are remnant artefacts from the adaptive grid refinement method which would need further adjustments (discussed in Sect. 5).

WL signatures
We focus first on the two right-hand side panels of these figures, where the distance of *PSP* is taken close to that of the April-
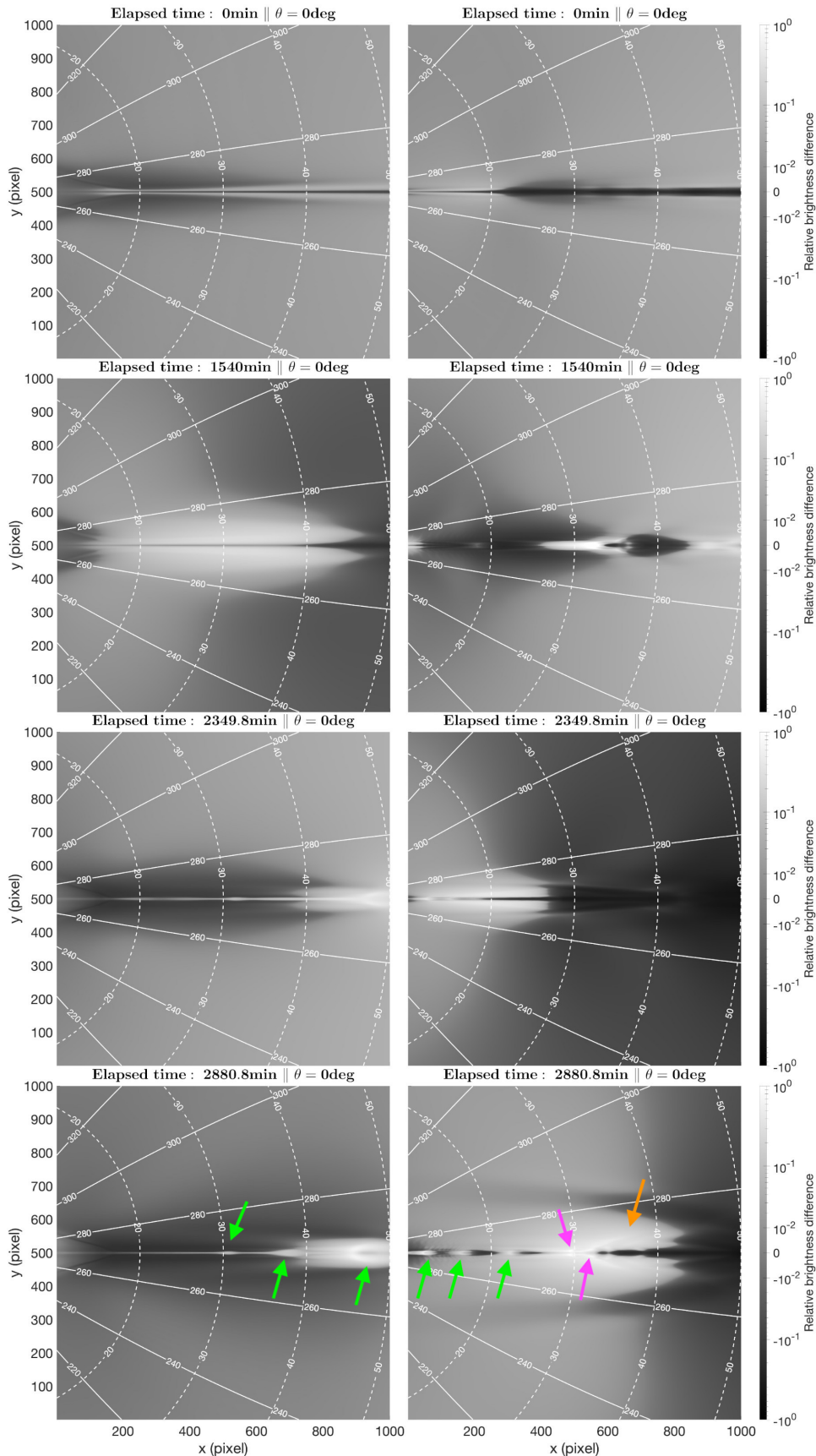
Fig. 8. Synthetic *WISPR-I* images produced from the idealistic dipolar setup introduced in Sect. 3.1, using a similar layout as Fig. 6, assuming that *PSP* is located at 10 R$_\odot$ (left column) and 35 R$_\odot$ (right column). Case of a flat streamer seen edge-on by *WISPR* ($\theta = 0°$). Colour plotted is the relative brightness difference with the mean brightness computed over the full interval, using a symmetrical logarithmic scale (with linear scale below a cut-off value of 10^{-2}). Isolines of the position and elongation (ϵ) angles (in degrees) are also plotted as solid and dashed white lines respectively. See the text for the colour coding of the arrows. An animated version of this figure is available online at https://doi.org/10.5281/zenodo.8135596.
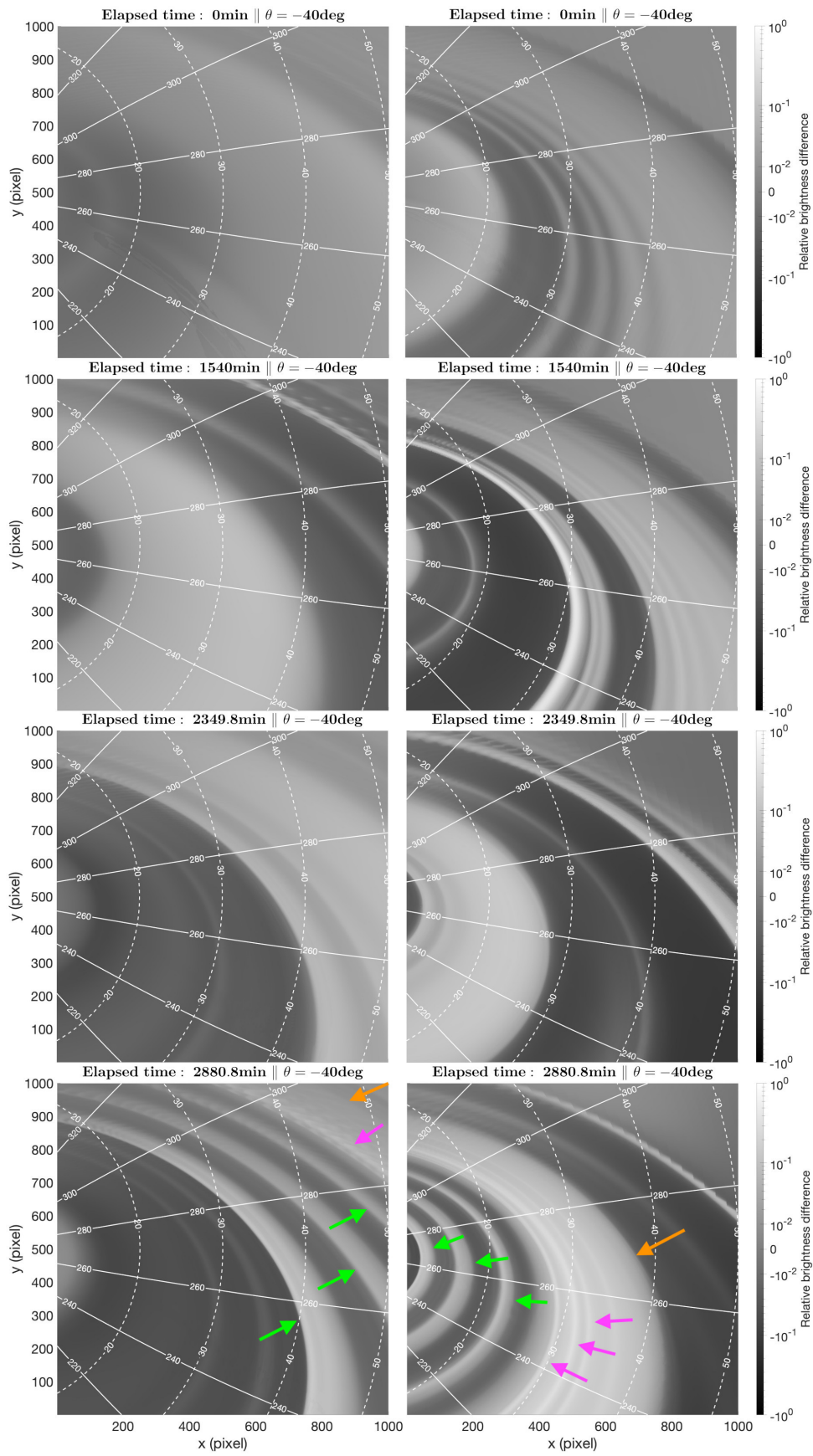
Fig. 9. Same as Fig. 8 but for the case of a flat streamer seen at a $\theta = -40°$ inclination angle by *WISPR*. An animated version of this figure is available online at https://doi.org/10.5281/zenodo.8135596.

2021 and March-2022 events observed by *WISPR* (i.e. 35 $R_\odot$). The four rows cover two full cycles of the development of the tearing instability. The $t = 2880.8$ min snapshot (bottom rows) is certainly the one that illustrates best the different phases. We can group the synthetic WL signatures in two main families:

1. *Bright diffuse patches that result from the main onsets of the tearing instability, that is the ballooning mode (see the orange arrows).* Due to their rather large scale, those are likely the so called streamer blobs that have long been observed from 1 AU, and first detected by *SoHO-LASCO* (Sheeley et al. 1997). When seen edge-on ($\theta = 0°$, Fig. 8) they show quite significant brightness enhancement of up to $\approx 35\%$, while when seen with some inclination ($\theta = -40°$, Fig. 9) they appear slightly dimmer with brightness enhancements below $\approx 10\%$. Because the simulated transients have here an infinite extent in azimuth, they show drifting signatures towards the FOV edges as they pass over *WISPR* location (see 2nd row of Fig. 8, right panel). That reminds us similar WL signatures that have been observed when *WISPR* approached and got through the streamer belt (Howard et al. 2019; Poirier et al. 2020), see also the simulations by Liewer et al. (2019). Nonetheless, having infinite azimuthal extents for such transients is not realistic, as clearly shown by the March-2022 event, and we will show in Sect. 4.2 that this can be solved using the full-fledged 3-D modelling setup.

2. *Bright and more concentrated emissions exhibiting quasi-periodic formation* (see the green and purple arrows). Similar spatial distributions and widths to that of both the April-2021 and March-2022 events observed by *WISPR* can be seen in the lower right panels of Figs. 8 and 9 respectively. These quasi-periodic structures develop at the back of the main onsets described just before, and can be connected to the long-observed hourly periodicities measured both remotely and in situ in the slow solar wind (Viall et al. 2010; Viall & Vourlidas 2015; Kepko et al. 2016). These structures are smaller in size than the streamer blobs discussed just above, and hence one would expect them to contribute less to the total brightness integrated along the LOS. Conversely, they exhibit much higher brightness enhancements because they contain a much higher concentration of plasma. Their brightness variation ranges $\approx 20 - 100\%$ (edge-on case, $\theta = 0°$, Fig. 8) and $\approx 1 - 40\%$ (face-on case, $\theta = -40°$, Fig. 9). Some of these structures propagate faster, and as a result happen sometimes to coalesce with their preceding fellows or even merge with the main onset (see the purple arrows).

In terms of brightness variation, there is a fair agreement between the simulated quasi-periodic structures and the transients observed by *WISPR*, that is $\approx 80 - 95\%$ for the April-2021 event (edge-on case, to be compared with $\theta = 0°$) and $\approx 30 - 50\%$ for the March-2022 event (face-on case, to be compared with $\theta = -40°$). On the other hand, the simulated ballooning modes (which can be associated to the Sheeley blobs) may be more difficult to see from *WISPR* perspective as their signature is fainter and more diffuse. They are also less likely to be detected by *WISPR* due to their long periodicity, as we shall see later in paragraph '*Periodicities*'.

Access to shorter heliocentric distances might help to better resolve both structures as illustrated in the left-hand side panels of Figs. 8-9, assuming the hypothetical $\simeq 10$ $R_\odot$ to be reached by *PSP* in 2024 at closest approach. There, the shrinking of the Thomson plateau (i.e. of the sensitive area of *WISPR*, see Sect. 3.3) should allow transients within streamers to more easily stand out from the background emissions. *WISPR* will also be able to observe these structures right in their formation region ($3 - 7$ $R_\odot$), and therefore might provide new clues about the tearing instability occurring at the HCS.

Propagation velocities and acceleration profiles
We now look at the kinematics of the simulated transients, by making J-maps as those shown in Fig. 4.

A synthetic J-map for the $\theta = 0°$ case is given in Fig. 10, where the slit has been taken at the solar equator (i.e. along the streamer). The $\theta = -40°$ case is not shown because it does not change much the rest of the analysis. We retrieve here the two main families of WL signatures identified in the previous section. First, the wide patches associated with the main onsets of the tearing instability (i.e. the ballooning mode), indicated by orange arrows again. Second, the more concentrated emissions associated with quasi-periodic transients, not pinpointed here as they clearly stand out as bright thin stripes from the rest.

The ballooning modes show quite different signatures in the J-map, with more curvature and less inclination. Their lower inclination indicates that they propagate at a slightly lower speed than the quasi-periodic structures, which are then likely to merge together as discussed previously. Their curvature may also be indicative of a more progressive acceleration until they reach their terminal speed after $\approx 10 - 15$ $R_\odot$, in contrast the fast quasi-periodic structures show clear constant speed profiles. Here the acceleration patterns are likely to be actual and not apparent accelerations as our *WISPR-I* FOV remains static in this simulation setup (see Sect. 3.3), although LOS-integration effects could still contribute to these curvatures as already discussed in Sect. 2.3. In both cases, the simulated transients reach a terminal speed of ≈ 250 km/s, that corresponds to the bulk-speed of the very slow and dense wind at the core of the streamer belt in the simulation.

Periodicities
The bottom panel of Fig. 10 shows the dominant periodicities over four full cycles of the tearing instability. The time elapsed in between each main onset of the tearing instability (i.e. the ballooning modes) is quite variable, reaching ≈ 25 hr between the first two and ≈ 50 hr for the others. That is here mostly driven by how fast helmet streamer loops can grow due to pressure imbalance, and hence is highly sensitive to local coronal conditions. This long periodicity is then likely to vary significantly from a simulation to another, and more generally over solar longitudes and along the solar cycle (see the discussion in Sect. 2.2). In comparison, a lower $\approx 8 - 16$ hr period had been detected from past *STEREO-A* observations (Sanchez-Diaz et al. 2017a), but this study focused on a few specific events around solar maximum of cycle 24. More recently, an analysis of the observations taken by the *STEREO-A COR-2* coronagraph near solar minimum has shown density variations in the streamer belt with timescales of 0.5-2 days (Morgan 2021), which this time agree with our simulation. Due to a fast and highly elliptical orbit *WISPR* is not appropriate to detect such long periodicities. Therefore, the legacy 1 AU observatories remain valuable assets, which in complement to the recently launched *Solar Orbiter* might finally allow us to better parameterize such events.

Regarding the quasi-periodic structures generated in between each main onset, a wavelet power spectrum (Torrence & Compo 1998) reveals dominant periods around $\approx 2 - 3$ hr $= 120 - 180$ min and $\approx 7 - 10$ hr. In addition, one may also notice that the simulation even exhibits some periodicities as low as ≈ 1.5 hr $= 90$ min (at $t = 100 - 105$ hr). These results are in good agreement with the $\approx 90 - 180$ min to $\approx 8 - 16$ hr periods
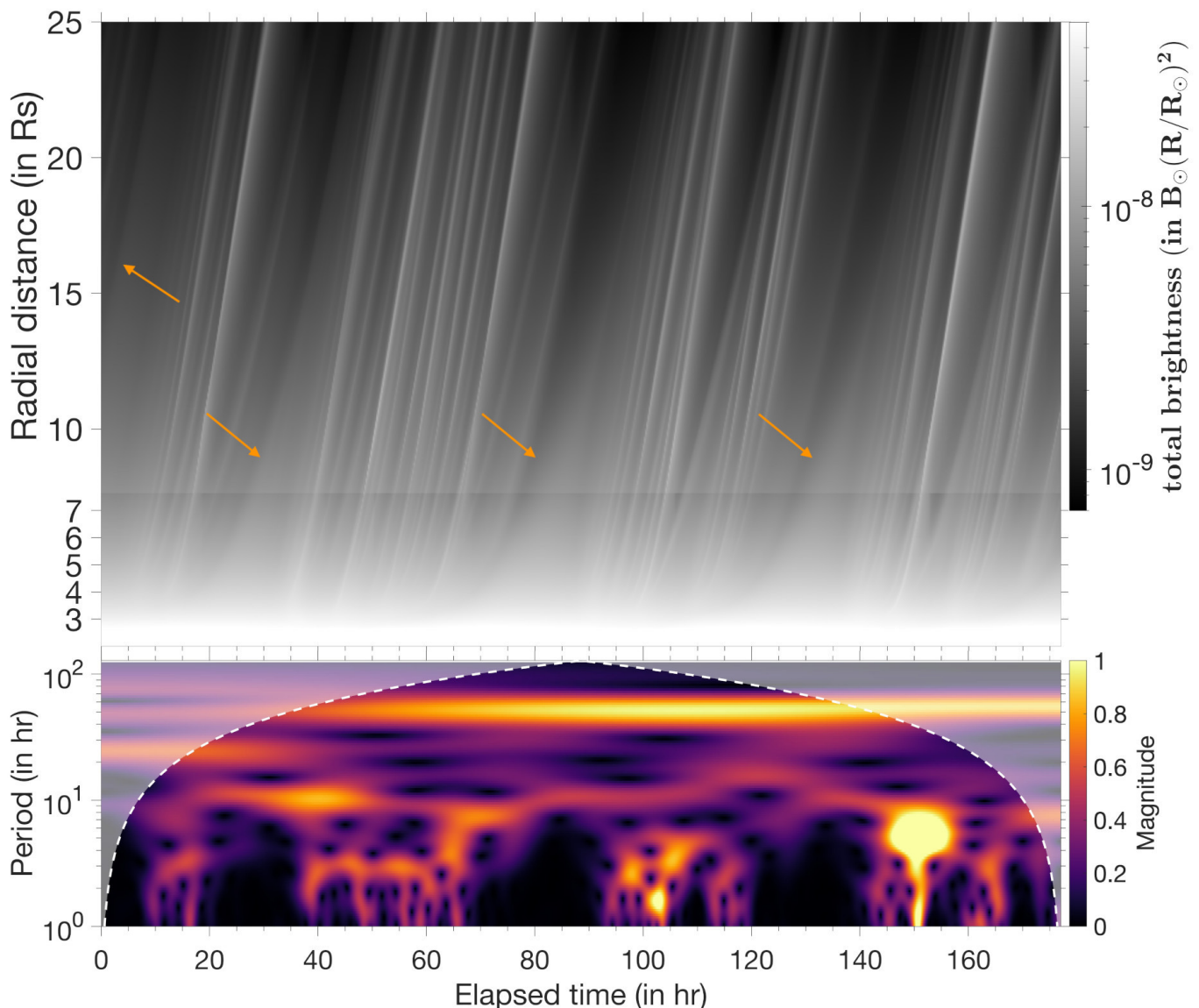
Fig. 10. Top panel: synthetic *WISPR-I* J-maps built from the two image sequences shown in Fig. 8 (case of a flat streamer seen edge-on by *WISPR*, $\theta = 0°$). Bottom panel: period decomposition at $r = 10\,R_\odot$ using a 1-D continuous wavelet transform (Morse wavelet).

that have been typically detected from 1 AU (Viall et al. 2010; Viall & Vourlidas 2015; Kepko et al. 2016; Sanchez-Diaz et al. 2017b). And more specifically, they also agree with those measured during the April-2021 ($130 - 175$ min), and March-2022 ($110 - 120$ min) events observed by *WISPR*.

4.2. Case study simulation of the 9th PSP encounter

We now exploit the full-fledged 3-D simulation setup introduced in Sect. 3.2 and detailed in Réville et al. (2022). Starting from April-2021 (8th encounter), interpreting *WISPR* observations has become highly challenging even with the use of such state-of-the-art modelling. That is primarily due to *PSP* diving much deeper inside the nascent solar wind and to an increase in the solar activity resulting in a much more structured corona. Tremendous efforts in tuning-up the model parameters would be required for a fair one-to-one comparison with the actual *WISPR* observations taken during the 9th encounter (August 2021). Also, a dynamic update of the magnetic map at the inner boundary would be essential to reach such goal. That is left for

future works, still there is a valuable set of information that we can extract from this simulation to feed the current discussion.

We present in figure 11 the result of our forward modelling method applied to this simulation. Similarly to Figs. 8-9, a difference method is used to better visualize brightness fluctuations due to transient propagating structures. But computing a mean background over the entire time interval is no more appropriate here, since our virtual *WISPR* observer is no more static. We then follow the well-known running difference method here, where the mean background image is computed over a sliding temporal window. For completeness and a more realistic impression, the raw synthetic products in absolute brightness are also shown in Fig. B.3.

Opposite to the idealistic modelling setup, a wealth of signatures are produced here with a rich diversity in shapes, extents and locations. They are indicated on Fig. 11 by coloured arrows which can be directly connected to the flux rope structures present in the simulation snapshot shown in Fig. 7. Transients can be seen all over the *WISPR-I/O* FOVs. In overall they show

great topological resemblances with the April-2021 and March-2022 events observed by *WISPR-I* (see Fig. 2). That is, arch-like (top panel) and blob-like (bottom panel) signatures representative of flux ropes seen face-on and edge-on respectively. This time, the full-fledged 3-D setup is more realistic with arch signatures of finite (and not infinite) spatial extent, because it includes secondary (or pseudo) streamer structures that were missing in the idealistic dipolar setup (see Sect. 3.2).

Furthermore, using Fig. 11 we can estimate that the simulated transients induce a similar increase in relative brightness of $\approx 1 - 4\%$ during their passage, although they are located a different distances from *WISPR*. These values are quite low compared to the brightness variations that have been estimated above from *WISPR* observations and the dipolar corona setup. This is because the background field is here computed over a much shorter temporal window, that is not well representative of the emissions from the background streamers. For this purpose we should use instead the raw synthetic images (in absolute brightness) that are shown in Fig. B.3, and compare the absolute brightness inside and just outside the transients (similarly to what we did for the real *WISPR* observations). By doing so we obtain more reasonable brightness variations of $\approx 8-17\%$.

Many of the brightness variations visible in Fig. 11 do not result from a propagating transient feature but to a change in the viewing conditions of *WISPR* as *PSP* flies rapidly along its orbit. That has been noticed many times by for instance the drift of streamer rays towards the FOV edges (Liewer et al. 2019; Howard et al. 2019; Poirier et al. 2020). This effect can be visualized in a supplementary movie provided with Fig. 11. Starting from August-09 2021, 18:37 UT, the movie shows the effect of *PSP* moving throughout the streamer belt, for the first time with a fully dynamic 3-D modelling setup that also includes the self-generation of streamer transient structures. As *WISPR* is getting closer to (and probably into) these imaged transients, their morphology changes quite significantly. That is both the consequence of a change in the perspective and of the sensitivity area of *WISPR* (see Sect. 3.3). Our comparison basis with actual observations can only be qualitative here for all the reasons mentioned before, such as the fact that the simulation does not cover the entire *WISPR* interval studied here (see Sect. 3.2). But still we could identify a lot of similarities between this synthetic movie and the newest *WISPR* observations starting from August 2021 (official movies for all *WISPR* observations can be found online[4]).

5. Discussion

In this study, we focused only on a few transient events observed by *WISPR*, that we considered as promising candidates produced by the streamer pinch-off reconnection mechanism. The April-26 and March-01 events have been especially hand-picked for their great visibility, but do not represent the full set of observations. *WISPR* observations show a plethora of transient features, in particular in the late *PSP* encounters (from September 2020 and on). Further studies are required to infer those transient properties in a statistical manner (see e.g. the upcoming paper from Viall & Vourlidas 2023).

Although the two modelling setups presented in this work show a great potential for interpreting some of the transient nature of *WISPR* images, there remains a lot to be improved still. Significant advances have been made in the forward modelling
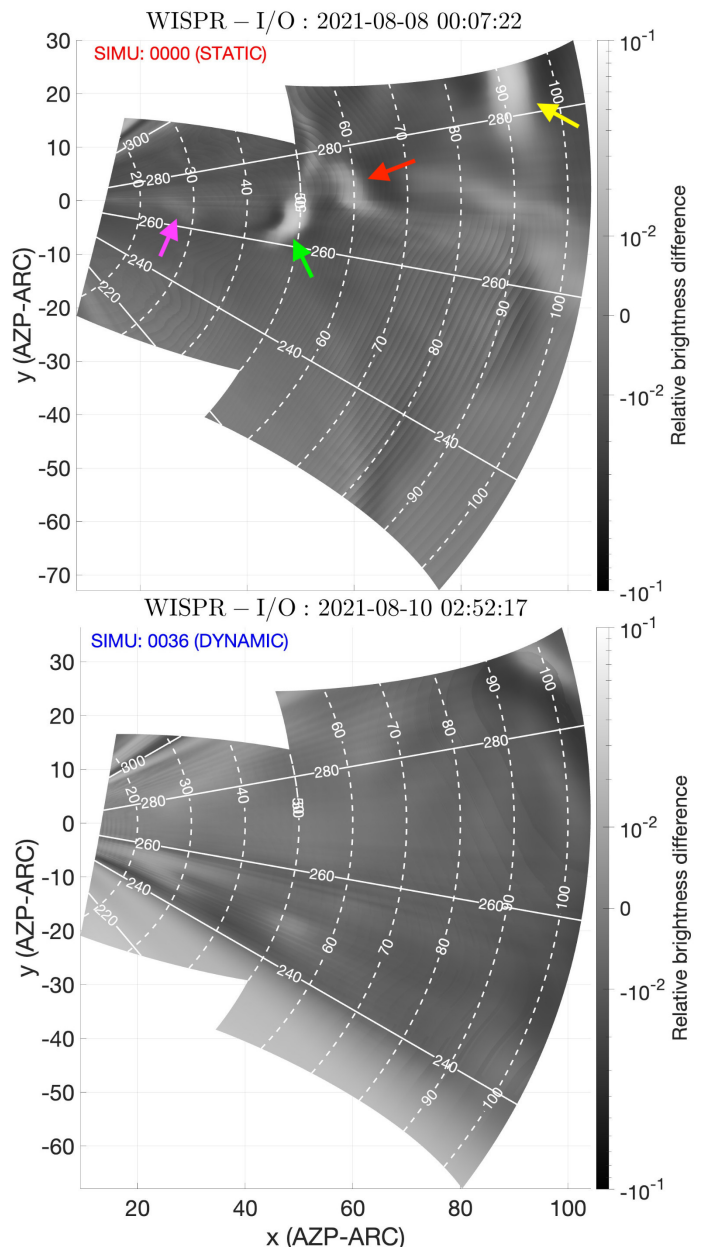
---

[4] https://wispr.nrl.navy.mil/encounter-summaries

Fig. 11. Synthetic images of both the inner *WISPR-I* and outer *WISPR-O* telescopes combined, produced with the full-fledged 3-D simulation setup introduced in Sect. 3.2. A mean background has been subtracted to each image using a sliding temporal window ranging $\approx 5 - 10$ hours (running difference method). The relative brightness difference to this mean background is colour plotted with a symmetrical logarithmic scale (with linear scale below a cut-off value of 10^0). As the simulation is ≈ 22 hour long, only a short temporal window around perihelion could be treated in a self-consistent manner (dynamic mode). Outside this dynamic interval, images have then been produced with either the first or last simulation snapshot (static mode). An animated version of this figure is available online at https://doi.org/10.5281/zenodo.8135596.

procedure compared to our previous study (Poirier et al. 2020), where most of the previous difficulties have been resolved. The adaptive grid refinement method allows for a much more accurate sampling of the LOS, that results in a very smooth rendering of small-scale density structures. Despite the high precision achieved, we still note some remaining artefacts of minor importance in the difference-based synthetic products. For the sake

of computational tractability, we had for each individual image to restrain the number of optimisation steps for the LOS sampling to a maximum (30 here). That implies that the optimisation procedure may not fully converge for all LOS, generating some spurious features sometimes.

These are minor inconveniences, and now the performance of our white-light rendering code is primarily limited by the quality of the input simulation. Future efforts should then concentrate on pushing existing solar coronal/wind models beyond their current capabilities in order to allow for a thorough understanding of the latest *WISPR* observations. In light with this work, below are some axes of progress that could be addressed:

– *Coronal structure fidelity*:
Current comparisons against *WISPR* observations greatly suffer from a misplacement of the main streamer belt and pseudo-streamer structures. That highlights the unique capability of *WISPR* to provide more stringent constrains to current coronal models. For instance the magnetic map set at the inner boundary is known to have a critical impact on the performance of existing MHD models. Having a magnetic map that is updated dynamically over time will be necessary improve comparisons with recent *WISPR* observations. On-going efforts have also been carried on towards a systematic benchmarking of MHD models against observations (see e.g. Badman et al. 2022), and *WISPR* observations could both greatly benefit from and support such works.

– *Spatial resolution*:
Although the full-fledged 3-D simulation setup depicts a much more realistic solar coronal structure, yet it only permits a partial development of the tearing instability compared to the idealistic but much more (spatially) resolved 2.5-D setup. Future works will have to refine the spatial resolution around the HCS further, but that is extremely challenging in such global 3-D MHD models while maintaining computational tractability.

– *Temporal cadence and duration*:
Together with a sufficiently spatially resolved model, temporal cadence is also important to track these streamer transients as they rapidly propagate throughout the *WISPR* FOV. That will be important especially in the years to come when *PSP* will sample these transients right in their formation region (i.e. the 10 $R_\odot$ case treated with the 2.5-D setup). Furthermore, simulation duration of more than one day would be preferable to maximize the scientific output. That can easily be achieved in a 2.5-D context but implies large amounts of data in full 3-D modelling setups, a challenge to reach with modern computational facilities.

6. Conclusion

The variability of the slow wind that originates from streamers has been analysed in light of the latest observations taken by *WISPR*. A few transient events have been identified with periodicities that are consistent with the previous $90 - 180$ min range detected from near 1 AU observations. The pinch-off reconnection mechanism occurring at the tip of helmet streamers has long been predicted as a potential source mechanism of these quasi-periodic structures.

For the first time, this work provides strong evidences to support this scenario using two advanced MHD models of the solar wind and corona, each of them having their own pros and cons. Both give rise to the same fundamental process though. First there is a thermal/pressure instability of the coronal loops that are lodged beneath the helmet streamers, that allows them to rise in the corona. They stretch to a point where the current sheet (HCS) that develops at their back becomes so thin that magnetic reconnection eventually occurs via the tearing instability. A large flux rope made of streamer material is then released (i.e. the main onset or ballooning mode), corresponding to the so called streamer blobs that have been first detected in *SoHO-LASCO*. Behind this main ejecta follows the further development of the tearing instability at the HCS, that generates a myriad of quasi-periodic smaller-scale structures. We stipulate that these quasi-periodic structures exhibit local density enhancements that are strong enough to be detected by *WISPR*, and that they actually show great topological similarities with two real events captured by *WISPR*. In addition, the simulated quasi-periodic structures have periodicities that agree well with these events, and also more generally with the $90 - 180$ min range detected in past observations.

These quasi-periodic structures could be reproduced in an idealistic dipolar setup thanks to a very high spatial resolution at the HCS. However, this setup lacked some consistency to simulate properly the actual WL signatures observed by *WISPR*. A global full-fledged 3-D MHD model was then necessary to simulate the aspect of these structures in a self-consistent manner. But then, the coarser spatial resolution did not allow for the full development of the tearing instability and thus of the quasi-periodic structures, where only the larger-scale structures resulting from the main onsets could be reproduced.

In any case, this work highlights the importance of the tearing instability occurring the tip of streamers, to fuel the long-observed high variability of the slow solar wind. Furthermore, we discuss of how extremely challenging the latest (and upcoming) *WISPR* observations remain to interpret even just for the quasi-steady component of the slow wind. That is because *PSP* is diving deeper and deeper within a solar corona that becomes highly structured with the rising phase of the solar cycle. Therefore *WISPR* offers new stringent constrains to push existing models of the solar corona and wind beyond their current capability, which in turn should help at better understanding *WISPR* observations.

Acknowledgements

References

Antiochos, S. K., Mikić, Z., Titov, V. S., Lionello, R., & Linker, J. A. 2011, The Astrophysical Journal, 731, 112

Arge, C. N., Henney, C. J., Hernandez, I. G., et al. 2013, in American Institute of Physics Conference Series, Vol. 1539, Solar Wind 13, ed. G. P. Zank, J. Borovsky, R. Bruno, J. Cirtain, S. Cranmer, H. Elliott, J. Giacalone, W. Gonzalez, G. Li, E. Marsch, E. Moebius, N. Pogorelov, J. Spann, & O. Verkhoglyadova, 11–14

Arge, C. N., Henney, C. J., Koller, J., et al. 2010, AIP Conference Proceedings, 1216, 343

Arge, C. N., Henney, C. J., Koller, J., et al. 2011, in Astronomical Society of the Pacific Conference Series, Vol. 444, 5th International Conference of Numerical Modeling of Space Plasma Flows (ASTRONUM 2010), ed. N. V. Pogorelov, E. Audit, & G. P. Zank, 99

Badman, S. T., Brooks, D. H., Poirier, N., et al. 2022, The Astrophysical Journal, 932, 135

Brooks, D. H. & Warren, H. P. 2011, The Astrophysical Journal Letters, 727, L13

Chen, Y., Li, X., Song, H. Q., et al. 2009, The Astrophysical Journal, 691, 1936

Cho, I.-H., Moon, Y.-J., Nakariakov, V. M., et al. 2018, Phys. Rev. Lett., 121, 075101

DeForest, C. E., Howard, R. A., Velli, M., Viall, N., & Vourlidas, A. 2018, The Astrophysical Journal, 862, 18

Domingo, V., Fleck, B., & Poland, A. I. 1995, Solar Physics, 162, 1

Dorfi, E. A. & Drury, L. O. 1987, Journal of Computational Physics, 69, 175

Doschek, G. A. & Warren, H. P. 2019, The Astrophysical Journal, 884, 158

Gibson, S. E., Kucera, T. A., White, S. M., et al. 2016, Frontiers in Astronomy and Space Sciences, 3

Gosling, J. T., Birn, J., & Hesse, M. 1995, Geophysical Research Letters, 22, 869

Hess, P., Howard, R. A., Stenborg, G., et al. 2021, Solar Physics, 296, 94

Hess, P., Rouillard, A. P., Kouloumvakos, A., et al. 2020, The Astrophysical Journal Supplement Series, 246, 25

Howard, R. A., Stenborg, G., Vourlidas, A., et al. 2022, ApJ, 936, 43

Howard, R. A., Vourlidas, A., Bothmer, V., et al. 2019, Nature, 576, 232

Howard, T. A. & DeForest, C. E. 2012, The Astrophysical Journal, 752, 130

Howard, T. A. & Tappin, S. J. 2009, Space Science Reviews, 147, 31

Kaiser, M. L., Kucera, T. A., Davila, J. M., et al. 2008, Space Science Reviews, 136, 5

Kasper, J. C., Abiad, R., Austin, G., et al. 2016, Space Sci. Rev., 204, 131

Kepko, L., Viall, N. M., Antiochos, S. K., et al. 2016, Geophysical Research Letters, 43, 4089

Ko, Y.-K., Raymond, J. C., Li, J., et al. 2002, The Astrophysical Journal, 578, 979

Korreck, K. E., Szabo, A., Nieves Chinchilla, T., et al. 2020, The Astrophysical Journal Supplement Series, 246, 69

Lavraud, B., Fargette, N., Réville, V., et al. 2020, The Astrophysical Journal Letters, 894, L19

Liewer, P., Vourlidas, A., Thernisien, A., et al. 2019, Solar Physics, 294, 93

Liewer, P. C., Neugebauer, M., & Zurbuchen, T. 2004, Solar Physics, 223, 209

Liewer, P. C., Qiu, J., Ark, F., et al. 2022, Sol. Phys., 297, 128

Liewer, P. C., Qiu, J., Penteado, P., et al. 2020, Sol. Phys., 295, 140

Lynch, B. J. 2020, The Astrophysical Journal, 905, 139

Morgan, H. 2021, ApJ, 922, 165

Morgan, H. & Cook, A. C. 2020, The Astrophysical Journal, 893, 57

Morgan, H., Jeska, L., & Leonard, D. 2013, ApJS, 206, 19

Neugebauer, M., Liewer, P. C., Smith, E. J., Skoug, R. M., & Zurbuchen, T. H. 2002, Journal of Geophysical Research (Space Physics), 107, 1488

Parenti, S., Réville, V., Brun, A. S., et al. 2022, ApJ, 929, 75

Peter, H. 1998, Astronomy and Astrophysics, 335, 691

Poirier, N., Kouloumvakos, A., Rouillard, A. P., et al. 2020, The Astrophysical Journal Supplement Series, 246, 60

Poirier, N., Rouillard, A. P., Kouloumvakos, A., et al. 2021, Frontiers in Astronomy and Space Sciences, 8, 84

Réville, V., Fargette, N., Rouillard, A. P., et al. 2022, Astronomy and Astrophysics, 659, A110

Réville, V., Velli, M., Rouillard, A. P., et al. 2020, The Astrophysical Journal Letters, 895, L20

Rouillard, A. P., Davies, J. A., Forsyth, R. J., et al. 2008, Geophys. Res. Lett., 35, L10110

Rouillard, A. P., Davies, J. A., Forsyth, R. J., et al. 2009a, Journal of Geophysical Research (Space Physics), 114, A07106

Rouillard, A. P., Kouloumvakos, A., Vourlidas, A., et al. 2020a, The Astrophysical Journal Supplement Series, 246, 37

Rouillard, A. P., Pinto, R. F., Vourlidas, A., et al. 2020b, Astronomy and Astrophysics, 642, A2

Rouillard, A. P., Poirier, N., Lavarra, M., et al. 2020c, The Astrophysical Journal Supplement Series, 246, 72

Rouillard, A. P., Savani, N. P., Davies, J. A., et al. 2009b, Solar Physics, 256, 307

Rouillard, A. P., Sheeley, N. R., J., Cooper, T. J., et al. 2011, The Astrophysical Journal, 734, 7

Sanchez-Diaz, E., Rouillard, A. P., Davies, J. A., et al. 2017a, The Astrophysical Journal, 851, 32

Sanchez-Diaz, E., Rouillard, A. P., Davies, J. A., et al. 2017b, The Astrophysical Journal Letters, 835, L7

Sanchez-Diaz, E., Rouillard, A. P., Lavraud, B., Kilpua, E., & Davies, J. A. 2019, The Astrophysical Journal, 882, 51

Sheeley, N. R., J., Herbst, A. D., Palatchi, C. A., et al. 2008, ApJ, 675, 853

Sheeley, N. R., J. & Rouillard, A. P. 2010, The Astrophysical Journal, 715, 300

Sheeley, N. R., J. & Wang, Y.-M. 2002, The Astrophysical Journal, 579, 874

Sheeley, N. R., Walters, J. H., Wang, Y. M., & Howard, R. A. 1999, J. Geophys. Res., 104, 24739

Sheeley, N. R., Wang, Y. M., Hawley, S. H., et al. 1997, The Astrophysical Journal, 484, 472

Stakhiv, M., Landi, E., Lepri, S. T., Oran, R., & Zurbuchen, T. H. 2015, The Astrophysical Journal, 801, 100

Stakhiv, M., Lepri, S. T., Landi, E., Tracy, P., & Zurbuchen, T. H. 2016, The Astrophysical Journal, 829, 117

Thernisien, A. F. & Howard, R. A. 2006, The Astrophysical Journal, 642, 523

Torrence, C. & Compo, G. P. 1998, Bulletin of the American Meteorological Society, 79, 61

Uchida, Y., McAllister, A., Strong, K. T., et al. 1992, PASJ, 44, L155

Viall, N. M., Kepko, L., & Spence, H. E. 2008, Journal of Geophysical Research (Space Physics), 113, A07101

Viall, N. M., Spence, H. E., Vourlidas, A., & Howard, R. 2010, Solar Physics, 267, 175

Viall, N. M. & Vourlidas, A. 2015, The Astrophysical Journal, 807, 176

Viall, N. M. & Vourlidas, A. 2023, in preparation

von Steiger, R. 1996, in Astronomical Society of the Pacific Conference Series, Vol. 109, Cool Stars, Stellar Systems, and the Sun, ed. R. Pallavicini & A. K. Dupree, 491

Vourlidas, A. & Howard, R. A. 2006, The Astrophysical Journal, 642, 1216

Vourlidas, A., Howard, R. A., Plunkett, S. P., et al. 2016, Space Science Reviews, 204, 83

Wang, Y. M., Sheeley, N. R., J., Walters, J. H., et al. 1998, The Astrophysical Journal Letters, 498, L165

Wang, Y. M., Sheeley, N. R., Socker, D. G., Howard, R. A., & Rich, N. B. 2000, Journal of Geophysical Research, 105, 25133

Webb, D. F. & Howard, T. A. 2012, Living Reviews in Solar Physics, 9, 3

Winterhalter, D., Smith, E. J., Burton, M. E., Murphy, N., & McComas, D. J. 1994, Journal of Geophysical Research, 99, 6667

Appendix A: Computational challenges and method

Having under resolved LOSs has been seen to have significant consequences on the synthetic images produced (including e.g. artefacts, missing density structures, see Poirier et al. 2020), and as such 121 points appeared to be sufficient to resolve the features studied in that previous work. However, the smallest density structures simulated in the idealistic dipolar setup introduced in Sect. 3.1, involve to resolve spatial structures of size as small as 0.1 $R_\odot$. As a consequence, running again our synthesizing script with 121 points only was no longer adequate. A significant improvement compared to our previous work (Poirier et al. 2020) has then been to push the LOSs resolution from 121 to 241 points, resulting in several computational challenges to tackle and which are discussed below.

Synthesizing a white-light image of 1000-by-1000 pixels implies to compute multiple 3-D matrices with up to 241 million elements each, for LOSs resolved with 241 points. In typical 32GB memory systems that quickly leads to an memory overflow. One main challenge has been to optimize the code so to minimise memory usage and by the meantime maximize the workload on CPUs. A prior step before actual computation is to break the image down to smaller sections, where the number of sections is adjusted automatically to ensure maximized performances. Each sub-section is then computed in parallel, hence using at most the capacity of current multi-core systems.

In theory the LOSs could be better resolved than 241 points, resulting in more sub-sections to compute and hence to a longer computational time. However, instead of adopting the 'brute' force by simply adding more points, we restrained ourselves to 241 points and worked on optimizing the point distribution along each LOS. To do so one needs to have a prior idea of which portions of the LOSs need to be better resolved than others. The Thomson scattering (introduced in subSect. 3.3) served as a basis to optimize the point distribution, following a two-step procedure described below.

1. We start by defining an uniform grid in scattering angle χ that covers both the foreground ($\chi = 90 \to \chi_{max}$) and background ($\chi = 90 \to \chi_{min}$) regions respectively, where $\chi_{min} = 0°$ and $\chi_{max} = 180° - \alpha$ are the asymptotic limits to the acceptable range of χ angles (α is the central angle between the LOS and the observer-Sun line). Using a χ-defined uniform grid is convenient as it naturally produces a non-uniform grid in the path length z (i.e. the distance along a LOS from observer position), with a minimum spatial step near the Thomson sphere. We make a first computation of the total brightness over this uniform grid. Before proceeding to the grid optimisation described afterwards, the spatial extent of each LOS is shrunk to a region that accounts for most (99% in this paper) of the total integrated brightness. The upper χ_u and lower χ_l limit to the integral of the total brightness (Eq. (1)) are determined when the ratio:

$$\mathcal{R} = \frac{\sum_{\chi=90°}^{\chi_{l,u}} n_e z^2 G dz}{\sum_{\chi=90°}^{\chi_{min,max}} n_e z^2 G dz} \tag{A.1}$$

reaches 0.99 in both the foreground and background regions. That allows us to save more grid points in needed areas and maximize the efficiency of the grid refinement step described in the next paragraph.

2. We then implemented an adaptive grid method following a similar approach as Dorfi & Drury (1987), where the spatial refinement adapts dynamically accordingly to the physical structures to be resolved, that is here the density structures along each LOS. For this purpose we define the grid point density by a function that includes the local distribution of the total (i.e. not polarized) WL intensity along each LOS:

$$R_i^{k+1} = \frac{1}{c} \sqrt{w_1 \left(\frac{\sum_{i=1}^{i=nlos} \Delta\chi_i^k}{\chi_u - \chi_l} \right)^2 + w_2 \left(\frac{I_{t,i}^k / \Delta z_i^k}{mean(I_{t,i}^k / \Delta z_i^k)} \right)^2} \tag{A.2}$$

$$c = \sqrt{w_1 + w_2}$$

where the lower i and upper k subscripts refer to the spatial and time indices respectively. That forms allows to apply multiple optimisation criteria pondered by their respective weights w_*, all chosen equal to one in this paper (after several tests having been made). First criterion (left term) allows us to constrain the extent of the optimised grid near the previously determined 99% range of interest. Second criterion purely depends on the studied physical system where more points are set where the local intensity is greater. One should make sure to use normalised quantities to get a proper balance between each criterion. As such, using the mean value of the integrated intensity $mean(I_t^k, i\Delta\chi_i^k)$ along each LOS appears to work best. Note that $w_2 = 0$ would lead to an uniform grid in χ. The actual spatial step in χ angle at the next temporal step is then determined by:

$$\Delta\chi_i^{k+1} = \Delta\chi_i^k \frac{R_i^k}{R_i^{k+1}} \tag{A.3}$$

This procedure is repeated iteratively until the total integrated brightness along all LOS converges to a stable value, defined as the relative brightness difference with previous iteration below $1e^{-2}$.

Appendix B: Raw synthetic products, absolute brightness

In terms of absolute brightness most of the transient signatures remain relatively faint over the background solar wind (see the coloured arrows in Figs. B.1-B.2), even though our virtual *WISPR* observer is imaging them from a very close distance. The idealistic case of an inclined streamer belt ($\theta = -40°$, Fig. B.2) is even dimmer compared to the LOS-aligned streamer belt case ($\theta = 0°$, Fig. B.1), as a much shorter portion of these transients is integrated along the LOS.

A similar comment can be made concerning the absolute brightness images synthesized from the full-fledged 3-D modelling setup (see Fig. B.3), for which the results are discussed in Sect. 4.2. Here only one flux rope structure barely stands out from the background.

For a better visualisation of these transients, we decided to work primarily with difference images as those shown in the core text.
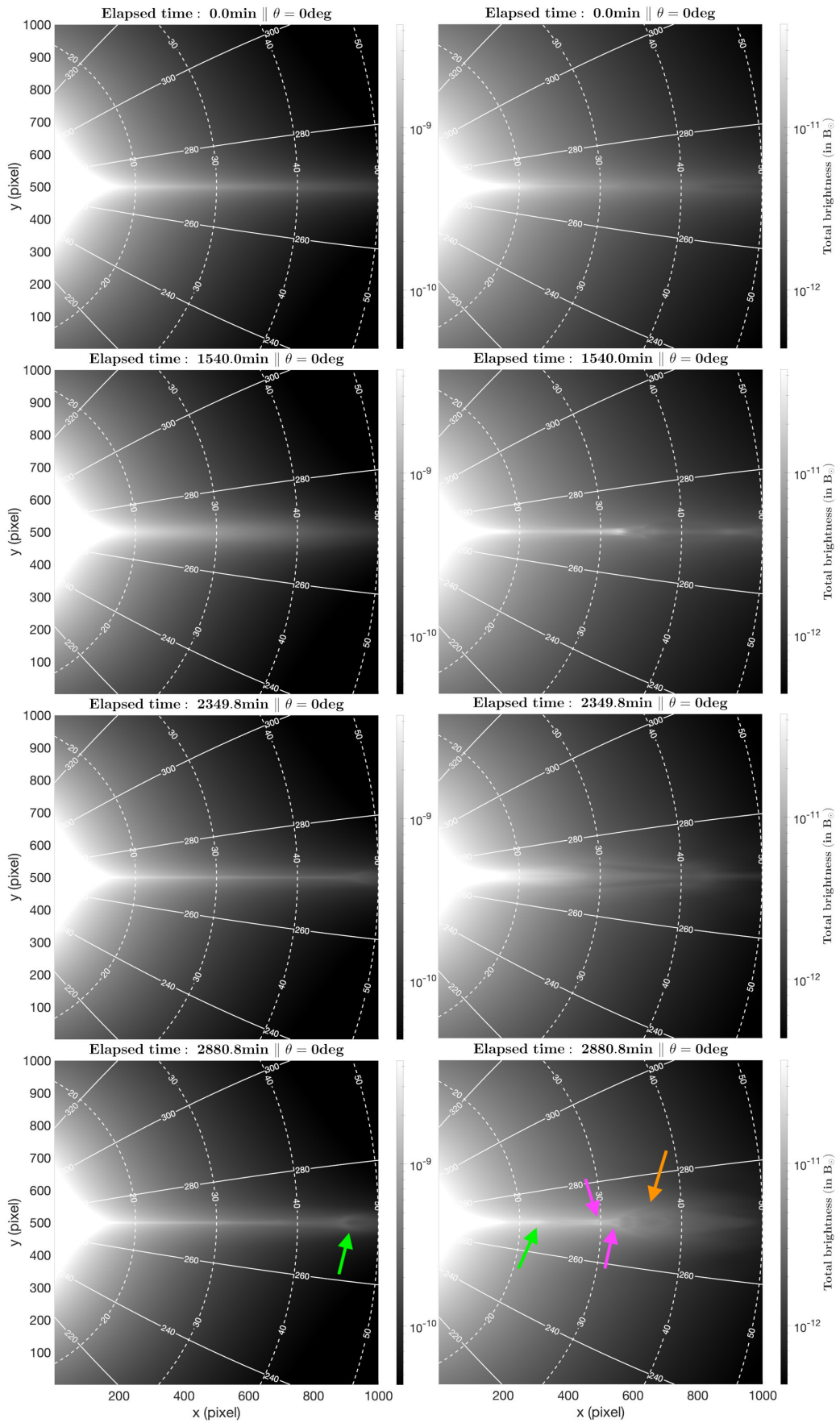
Fig. B.1. Same as Fig. 8 but for the absolute brightness, plotted in unit of mean solar brightness $B_\odot = 2.3e7$ W.m^{-2}.sr^{-1} and in a logarithmic scale. An animated version of this figure is available online at https://doi.org/10.5281/zenodo.8135596.
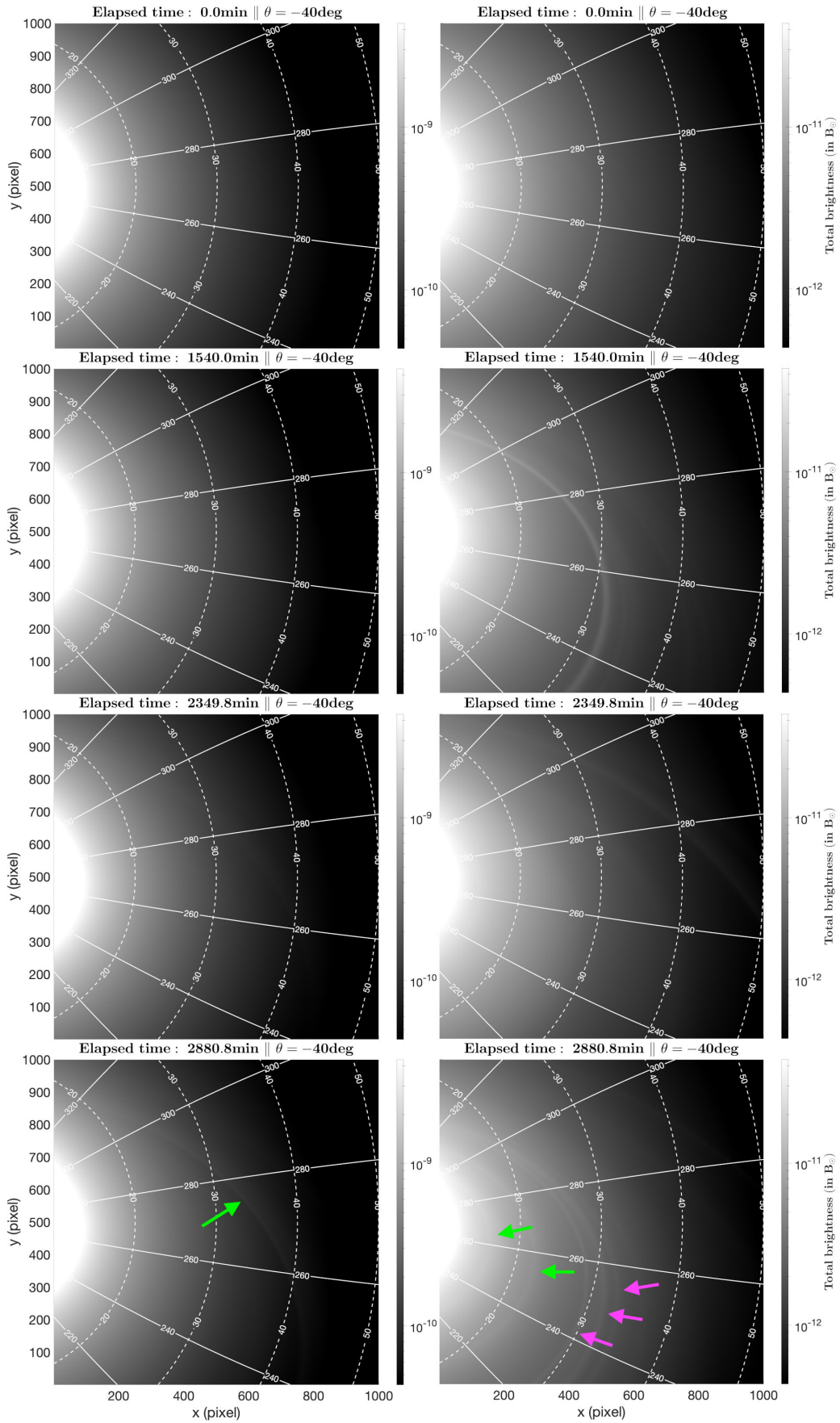
Fig. B.2. Same as Fig. 9 but for the absolute brightness, plotted in unit of mean solar brightness $B_\odot = 2.3e7$ W.m^{-2}.sr^{-1} and in a logarithmic scale. An animated version of this figure is available online at https://doi.org/10.5281/zenodo.8135596.
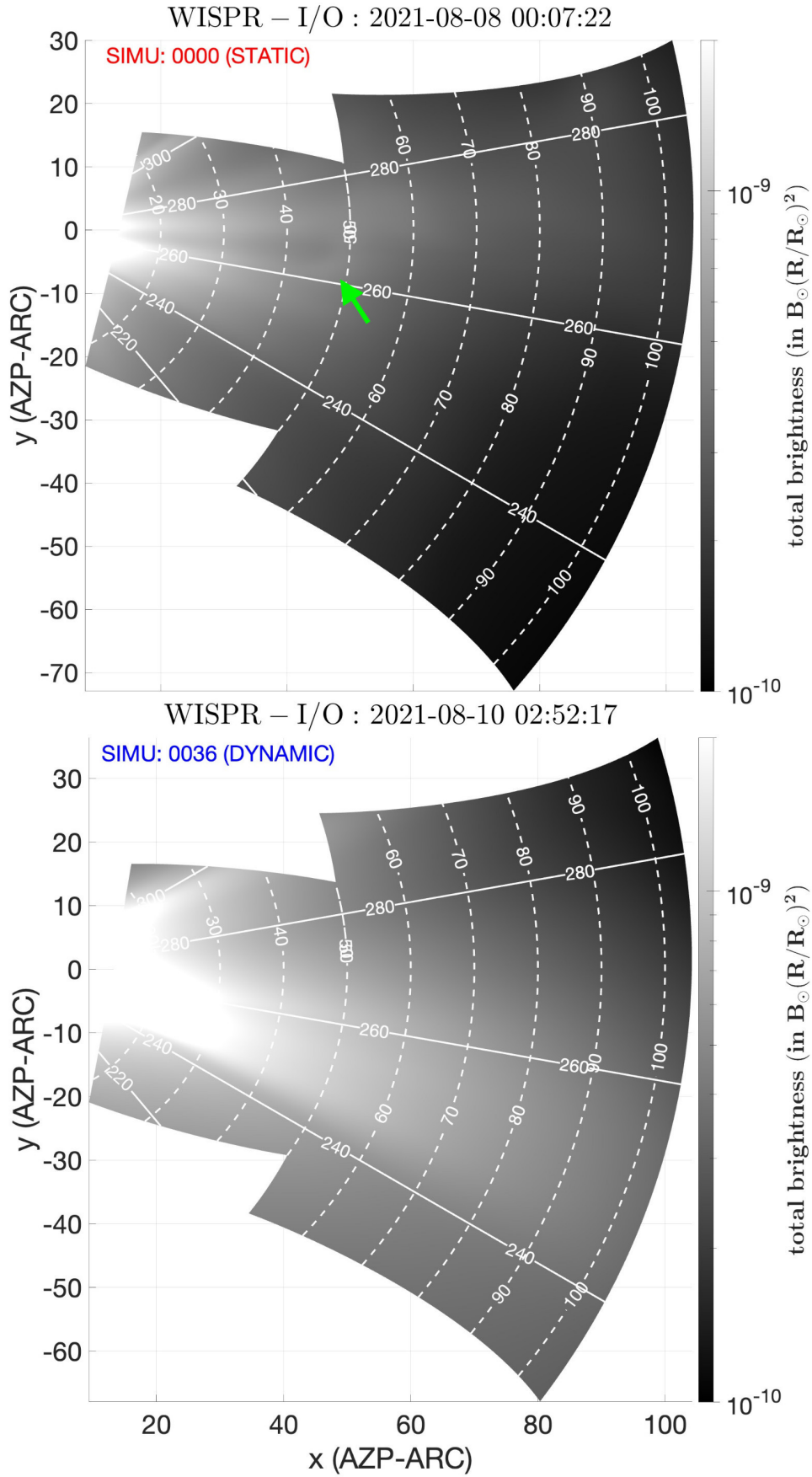
Fig. B.3. Same as Fig. 11 but for the absolute brightness, plotted in unit of mean solar brightness $B_\odot = 2.3e7$ W.m^{-2}.sr^{-1} scaled with the square of the radial distance $B_\odot(R/R_\odot)^2$, and in a logarithmic scale. An animated version of this figure is available online at `https://doi.org/10.5281/zenodo.8135596`.